

# Geochemistry, Geophysics, Geosystems®

## RESEARCH ARTICLE

10.1029/2021GC010206

### Special Section:

Insights into Subduction Zone Processes from Models and Observations of Exhumed Terranes

### Key Points:

- Fluid-mediated mass transfer between mafic and ultramafic rocks can occur from prograde to peak, to retrograde conditions
- The formation of chlorite-rich assemblages through Mg metasomatism of mafic rocks is prevalent at high  $P$ - $T$  conditions
- Talc formation via Si-metasomatism of serpentinite is more limited in subduction zones than in oceanic plates

### Supporting Information:

Supporting Information may be found in the online version of this article.

### Correspondence to:

E. A. Codillo,  
ecodillo@mit.edu

### Citation:





Codillo, E. A., Klein, F., Dragovic, B., Marschall, H. R., Baxter, E., Scambelluri, M., & Schwarzenbach, E. (2022). Fluid-mediated mass transfer between mafic and ultramafic rocks in subduction zones. *Geochemistry, Geophysics, Geosystems*, 23, e2021GC010206. <https://doi.org/10.1029/2021GC010206>

Received 8 OCT 2021  
Accepted 17 JUN 2022

© 2022. The Authors.

This is an open access article under the terms of the [Creative Commons Attribution License](#), which permits use, distribution and reproduction in any medium, provided the original work is properly cited.

## Fluid-Mediated Mass Transfer Between Mafic and Ultramafic Rocks in Subduction Zones

E. A. Codillo<sup>1,2</sup> , F. Klein<sup>3</sup> , B. Dragovic<sup>4</sup>, H. R. Marschall<sup>2,5</sup> , E. Baxter<sup>6</sup>, M. Scambelluri<sup>7</sup>, and E. Schwarzenbach<sup>8</sup> 

<sup>1</sup>Massachusetts Institute of Technology-Woods Hole Oceanographic Institution Joint Program in Oceanography/Applied Ocean Science and Engineering, Woods Hole, MA, USA, <sup>2</sup>Department of Geology and Geophysics, Woods Hole Oceanographic Institution, Woods Hole, MA, USA, <sup>3</sup>Department of Marine Chemistry and Geochemistry, Woods Hole Oceanographic Institution, Woods Hole, MA, USA, <sup>4</sup>School of the Earth, Ocean & Environment, University of South Carolina, Columbia, SC, USA, <sup>5</sup>Institut für Geowissenschaften, Goethe Universität Frankfurt, Frankfurt, Germany, <sup>6</sup>Department of Earth and Environmental Sciences, Boston College, Newton, MA, USA, <sup>7</sup>Department of Earth Sciences, University of Genova, Genova, Italy, <sup>8</sup>Institut für Geologische Wissenschaften, Freie Universität Berlin, Berlin, Germany

**Abstract** Metasomatic reaction zones between mafic and ultramafic rocks exhumed from subduction zones provide a window into mass-transfer processes at high pressure. However, accurate interpretation of the rock record requires distinguishing high-pressure metasomatic processes from inherited oceanic signatures prior to subduction. We integrated constraints from bulk-rock geochemical compositions and petrophysical properties, mineral chemistry, and thermodynamic modeling to understand the formation of reaction zones between juxtaposed metagabbro and serpentinite as exemplified by the Voltri Massif (Ligurian Alps, Italy). Distinct zones of variably metasomatized metagabbro are dominated by chlorite, amphibole, clinopyroxene, epidote, rutile, ilmenite, and titanite between serpentinite and eclogitic metagabbro. Whereas the precursor serpentinite and oxide gabbro formed and were likely already in contact in an oceanic setting, the reaction zones formed by diffusional Mg-metasomatism between the two rocks from prograde to peak, to retrograde conditions in a subduction zone. Metasomatism of mafic rocks by Mg-rich fluids that previously equilibrated with serpentinite could be widespread along the subduction interface, within the subducted slab, and the mantle wedge. Furthermore, the models predict that talc formation by Si-metasomatism of serpentinite in subduction zones is limited by pressure-dependent increase in the silica activity buffered by the serpentine-talc equilibrium. Elevated activities of aqueous Ca and Al species would also favor the formation of chlorite and garnet. Accordingly, unusual conditions or processes would be required to stabilize abundant talc at high  $P$ - $T$  conditions. Alternatively, a different set of mineral assemblages, such as serpentine- or chlorite-rich rocks, may be controlling the coupling-decoupling transition of the plate interface.

## 1. Introduction

The release of aqueous fluids from subducted sediments, altered oceanic crust, and serpentinized mantle is a fundamental process that drives arc volcanism, and facilitates the recycling of volatile and redox components from the solid Earth back to the ocean and atmosphere. Key to this understanding lies on the processes that set or modify the bulk compositions of subducted materials from oceanic settings up to subduction zones. Oceanic rocks and sediments are often subjected to combined, and sometimes coeval, deformation processes and fluid-rock interactions that can significantly modify their petrophysical (e.g., density, magnetic susceptibility), geochemical (e.g., trace elements, water and other volatiles), and redox properties prior to subduction. Important examples of these processes include serpentinization, carbonation, and talc-alteration of mantle rocks, as well as rodingitization, chloritization, and epidotization of mafic rocks (Bach et al., 2004; Bach & Klein, 2009; Honnorez & Kirst, 1975; Humphris & Thompson, 1978; Klein et al., 2009; Schwarzenbach et al., 2021). During subduction and exhumation, fluid-rock interactions at higher pressure and temperature conditions can further modify their geochemical, petrophysical, and redox characteristics. This is supported by field-based observations from exhumed high-pressure rocks in subduction zones worldwide (Bebout & Barton, 2002; Bebout & Penniston-Dorland, 2016; Breeding et al., 2004; Fryer, 2012; Gorman et al., 2019; Gyomlai et al., 2021; Harlow et al., 2016; Marschall et al., 2009; Pogge von Strandmann et al., 2015; Sorensen & Grossman, 1989).

Exhumed high-pressure terranes offer critical insights into the chemical interactions between disparate lithologies in subduction zones (notably serpentinites, eclogites, and metasedimentary rocks) that can produce complex reaction zones. However, accurate interpretation of such complex terranes requires distinguishing the signatures of high-pressure metasomatic processes in subduction zones from reworking and incomplete preservation during exhumation, and from inherited oceanic alteration prior to subduction (Bebout, 2007). This task is often challenging as some of the same mineral assemblages can form in low-pressure oceanic and high-pressure subduction zone settings. For instance, hydrous mineral assemblages containing chlorite  $\pm$  amphibole  $\pm$  serpentine  $\pm$  talc, which dominate the exhumed high-pressure metasomatic rocks in Syros (Greece), Santa Catalina Island (USA), New Caledonia, and many other high-pressure localities, also exist in low-pressure oceanic environments (Bach et al., 2004; Bebout & Barton, 2002; Boschi et al., 2006; Miller et al., 2009; Paulick et al., 2006; Spandler et al., 2008). This makes it difficult to determine the conditions and tectonic setting of mass transfer recorded by exhumed high-pressure terranes and adds uncertainty to the quantification of mass transfer in subduction zones. Importantly, as metasomatic interactions can occur at forearc to subarc depths, they are believed to profoundly influence arc magmatism and seismicity of the subducted slabs (Abers et al., 2006; Angiboust et al., 2012; Kirby et al., 2013; Marschall & Schumacher, 2012). Such metasomatic processes, though hidden from sight, are likely to be operational and pervasive at depth.

This study employs a multi-pronged approach to assess mass transfer between mafic and ultramafic rocks in subduction zones, using the high-pressure Voltri Massif (Ligurian Alps, Italy) as a natural laboratory. To that end, we integrate petrography, bulk-rock and mineral chemistry, radiogenic Sr isotopes, and petrophysical properties, with thermodynamic phase equilibria and reaction-path modeling to constrain how, where, and when metasomatism occurred. We demonstrate that fluid-mediated mass transfer was dominated by Mg from serpentinite to metagabbro at high-pressure, which lead to substantial mineralogical, chemical, and petrophysical changes. We discuss the geological implications of metasomatism for subduction environments where mafic and ultramafic rocks are juxtaposed, such as the slab-mantle interface, the mantle wedge, and within the subducting slab.

### 1.1. Geological Background

Located in the Ligurian Alps of Italy, the Voltri Massif is composed of distinct tectonic slices of meta-ophiolitic rocks, oceanic metasediments, continent-derived plutonic rocks and metasediments, and oceanic mantle of subcontinental lithospheric origin. The whole massif records a complex tectonic history. The metamorphosed materials represent slivers of ocean floor formed during seafloor spreading in the former Liguro-Piedmont ocean in the Late Jurassic. This ocean floor was later subducted during the convergence of Europe and Adria in the Early Cretaceous about 25 Ma after cessation of the oceanic spreading (Hunziker, 1974) to reach peak eclogite-facies conditions, and locally these lithologies experienced subsequent minor greenschist-facies overprint during exhumation (Federico et al., 2005, 2007; Malatesta et al., 2012a; Messiga & Scambelluri, 1991; Rampone & Hofmann, 2012; Vignaroli et al., 2005). However, diverging views of the tectonic origins of rocks exposed in the Voltri Massif prevail in the literature. The presence of rodingites embedded within serpentines was interpreted to indicate pre-subduction metasomatism of mafic oceanic crust (Piccardo, 2013; Scambelluri & Rampone, 1999). Accordingly, the structural, stratigraphic, and compositional relationships observed in the Voltri Massif were, to some extent, inherited signatures on the seafloor prior to subduction. However, additional alteration and mass transfer at high-pressure conditions were noted for some of the tectonic units in the Western Alps (e.g., Monviso Unit, the Cascine Parasi mélange of the Voltri Massif) on the basis of petrologic, field structural, and thermobarometric evidence (Federico et al., 2015; Guillot et al., 2009; Malatesta et al., 2012a). For instance, structural aspects (i.e., block-in-matrix facies of meta-crustal blocks within serpentinite domains) and heterogeneous peak metamorphic conditions recorded by different meta-crustal blocks within the massif led Malatesta et al. (2012a), Malatesta et al. (2012b) to suggest that the Voltri could be an exhumed sliver of a “fossil” serpentinite subduction channel mélange at the slab-mantle interface (Gerya & Stöckhert, 2006; Gerya & Yuen, 2003). The hydrous mineral assemblages (e.g., chlorite, Ca-amphibole, epidote) sandwiched in between eclogites and serpentinites were proposed to have formed during the blueschist-to greenschist-facies retrograde exhumation (Federico et al., 2007; Malatesta et al., 2012a). A recent study investigated the *P-T*-time evolution and bulk Sm-Nd garnet ages of different high-pressure (HP) mafic rocks in the Voltri Massif to determine whether these mafic rocks were indeed exhumed as blocks within a chaotic mélange or as coherent sections of oceanic lithosphere (Starr et al., 2020). Different from previous studies (e.g., Federico et al., 2007; Malatesta et al., 2012a, 2012b) it was suggested that a significant portion of the Voltri Massif was exhumed as large

kilometric-scale coherent sections of ultramafic and mafic slab material (Cannaò et al., 2016; Smye et al., 2021; Starr et al., 2020). A more detailed assessment of the structural aspects of the entire Voltri Massif is discussed elsewhere (Federico et al., 2007, 2015; Malatesta et al., 2012a).

Our study focuses on the Voltri Massif, which is mainly composed of eclogite-facies metagabbro, metabasalt and metasediment enclosed in highly schistose serpentinites. The Voltri metagabbro crops out as meter-scale blocks mostly derived from precursor Fe-Ti gabbros surrounded by highly schistose serpentinites and chlorite schists. Metagabbro derived from Fe-Ti gabbros show higher garnet modal abundance compared with Mg-Al gabbro derivatives. A late stage retrograde greenschist facies assemblage (chlorite + actinolite + albite + quartz) partially replaced the eclogite-facies assemblage (Malatesta et al., 2012a; Vignaroli et al., 2005). Previous studies of high-pressure serpentinite at Voltri have documented a foliation in serpentinite that is generally parallel to the garnet-pyroxene foliation observed in adjacent eclogitic blocks (Cannaò et al., 2016; Federico et al., 2007; Haws et al., 2021; Malatesta et al., 2012a). Furthermore, a range of prograde to peak metamorphic conditions from 1.8 to 2.4 GPa and 500–600°C occurring at ~50–33 Ma, followed by partial retrogression through blueschist (~1.2 GPa and 550°C) and greenschist-facies conditions (~0.8 GPa and 480°C) occurring at ~34–24 Ma have been proposed for the Voltri Massif metagabbros (Messiga et al., 1983; Messiga & Scambelluri, 1991; Smye et al., 2021; Starr et al., 2020; Vignaroli et al., 2005).

## 2. Materials and Methods

We sampled a transect across metasomatic reaction zones between juxtaposed serpentinite and eclogite-facies metagabbro (Figure 1a). This transect represents a traverse across a single, continuous metagabbro block into the surrounding serpentinite (N 44.478, E 8.599, 630 m above sea level; Figure S1 in Supporting Information S2). There is no field evidence for multiple dismembered metacrustal blocks in the sampled transect. The timing of peak metamorphism of the eclogitic metagabbro block sampled in this study was previously constrained at ~40 Ma using Sm-Nd garnet geochronology (metagabbro block 3; Starr et al., 2020). A total of 22 discrete samples were collected using a diamond-tipped rock drill, covering >3 m on the serpentinite side and ~1 m on the eclogitic metagabbro side relative to the original lithologic contact. Serpentinite and eclogitic metagabbro samples farthest away from the contact were chosen to represent rocks that are presumably the least affected by mass transfer processes. Caution was implemented during the selection of rocks to avoid weathered surfaces. Samples were classified into five zones based largely on mineralogy as follows: Zone I (samples V17-X808B14 to B22), Zone II (samples V17-X808B12 and V17-X808B13), Zone III (samples V17-X808B01 to B03), Zone IV (samples V17-X808B04 to V17-X808B08) and Zone V (samples V17-X808B09 and V17-X808B10). Henceforth, these samples will be referred to as for example, “B01” for sample V17-X808B01, etc. In the field, serpentinite (Zone I) is separated from metagabbro (Zones II–V) by a sharp lithologic contact that can be traced laterally along the stretch of the outcrop. Zone II is distinguished in the field by its flaky appearance and is mainly composed of amphibole and chlorite with a foliation that is more apparent than in Zones III to V. The transitions between metasomatic reaction zones in the metagabbro are gradational, and distinguished primarily based on mineralogy (Figure 1a). Samples were inspected in transmitted and reflected light using a Zeiss AxioImager 2 microscope, with mineral identification and abundance estimates complemented by scanning electron microscopy (SEM), confocal Raman spectroscopy, electron microprobe analysis (EPMA), and thermogravimetric analysis (TGA). Loss on ignition of bulk rock samples were also determined using TGA (see supplementary material).

We performed equilibrium thermodynamic modeling of representative bulk compositions coupled with garnet isopleth modeling to provide constraints on the pressure and temperature conditions of mass transfer. Pseudosections were computed using the program *Perple\_X* (version 6.9.0; Connolly, 2009) and the internally consistent dataset (version 5.5) of Holland and Powell (1998) in the MnO-Na<sub>2</sub>O-CaO-FeO-MgO-Al<sub>2</sub>O<sub>3</sub>-SiO<sub>2</sub>-H<sub>2</sub>O-TiO<sub>2</sub>-O<sub>2</sub> (MnNCFMASHTO) chemical system. Thermodynamic reaction-path models were developed using the EQ3/6 software package (Wolery, 1992) and the Deep Earth Water (DEW) Model (Huang & Sverjensky, 2019; Sverjensky, 2019; Sverjensky et al., 2014) database to aid in the interpretation of fluid-rock interactions. In particular, we used reaction-path modeling to further assess the alteration history and concomitant mineralogical changes during a fluid-mediated reaction between hydrated ultramafic (serpentinites) and metamorphosed crustal rocks (metagabbro) at subduction-zone conditions guided by *P-T* constraints from equilibrium pseudosection and garnet isopleth models. Results of reaction-path models were compared to the sequence of mineral assemblages



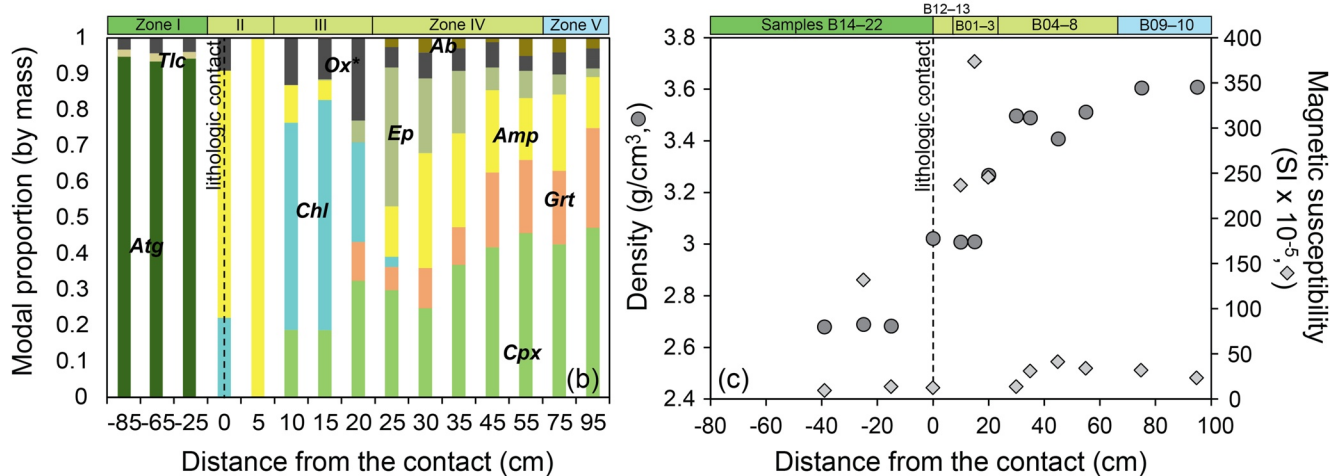
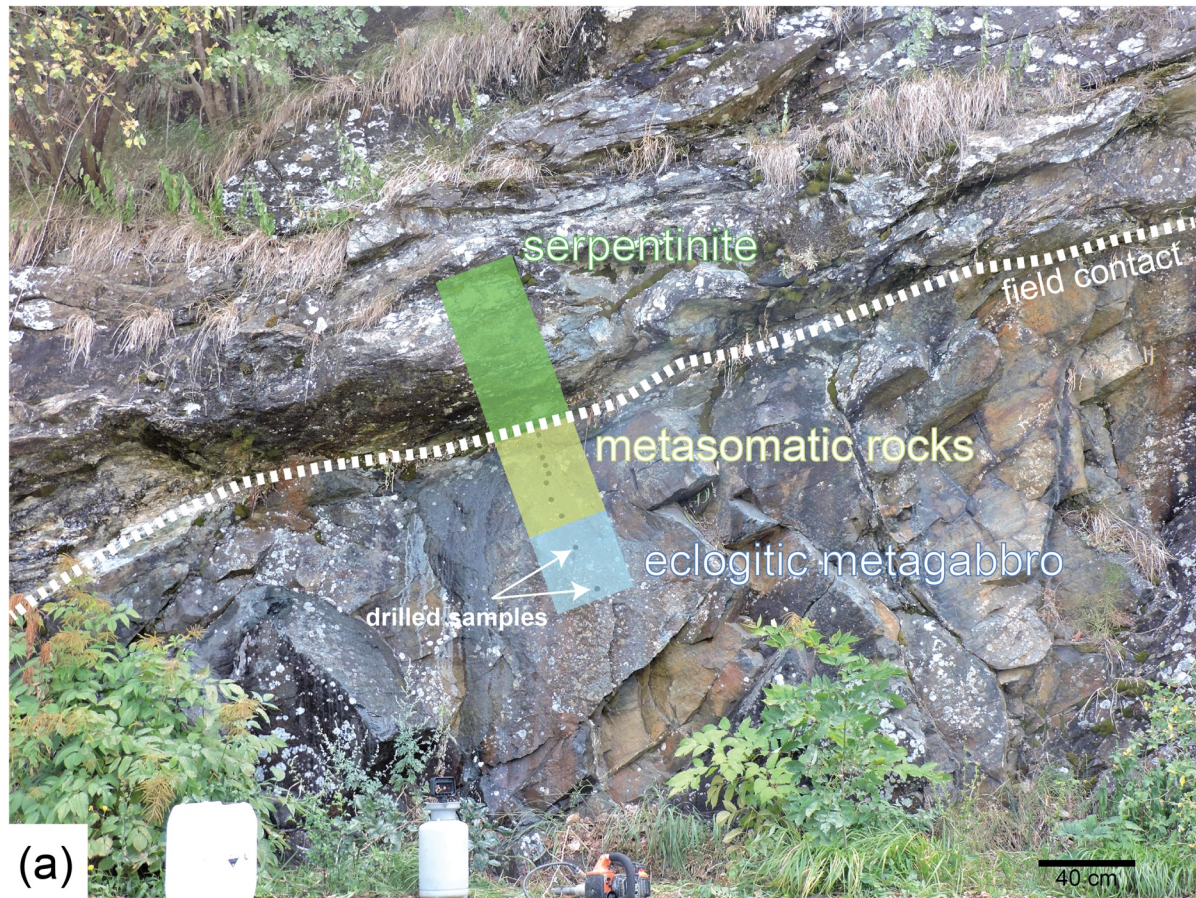


**Figure 1.** Outcrop examined in this study (a) Photograph of the sampled transect between serpentinite and metagabbro in the Voltri Massif. Circles indicate the locations where samples for this study were drilled out of the eclogite. The two lithologies were separated by a sharp lithologic contact that can be traced laterally along the stretch of the outcrop. Samples from serpentinite side were taken either by hand or by drilling in a region that is offset ~4 m to the left of the eclogite transect (not visible in this photo) which extends to ~2.25 m from the field contact between eclogite and serpentinite (white dashed line). The subdivision into eclogitic metagabbro, metasomatic rocks (reaction zones), and serpentinite is indicated by different colored regions. Zone II is distinguished in the field by its relatively weak and flaky consistency with foliation more pronounced than in Zones III–V. The mineralogical transitions from Zones III to V in the metagabbro block are diffuse and gradational. (b) Modal mineralogy, (c) bulk density and magnetic susceptibility across the serpentinite–metagabbro transect. Mineral proportions are given in fraction by mass, as calculated from thin-section chemical maps, coupled with modal estimates from mass-balance calculations using mineral and whole-rock compositions. Modal proportions of ilmenite, rutile, as well as their common replacement mineral titanite, were grouped and represented by Ox\*. Note that the modal estimate at the contact (zero distance) was based on field observations, bulk composition, and TGA–DSC analysis.



from petrographic observations. Detailed descriptions of the analytical techniques and the setup for thermodynamic phase equilibria and reaction-path modeling are provided in the supplementary material (Codillo, 2022).

### 3. Results

The mineral modal abundances, spatial distributions, and bulk petrophysical properties of the metasomatic reaction zones between the serpentinite and eclogitic metagabbro are shown in Figure 1 and reported along with bulk-rock major and trace-element concentrations,  $^{87}\text{Sr}/^{86}\text{Sr}$  isotope ratios, and bulk-rock  $\text{Fe(III)}/\text{Fe}_T$  in the supplementary table. Note that the full extent of the reaction zone highlighted was not immediately apparent in the field. Based on petrographic and spectroscopic characterization, coupled with mineral chemical data and TGA-DSC measurements, we distinguish Zone I (antigorite + magnetite serpentinite), Zone II (chlorite + Ca-amphibole-rich metagabbro), Zone III (chlorite-rich metagabbro), Zone IV (epidote + Na-Ca amphibole-rich metagabbro), and Zone V (eclogitic metagabbro). The sharp lithologic-tectonic contact that separates the serpentinites and metagabbro is located in between Zones I and II. Zones II to IV consist of variably altered metagabbro with distinct mineralogical assemblages, sandwiched in between serpentinite (Zone I) and distal eclogitic metagabbro (Zone V). Consistent with previous findings (Cannaò et al., 2016; Haws et al., 2021; Malatesta et al., 2012a), the foliation in serpentinite is generally parallel to the foliation in the adjacent metagabbro block. A detailed assessment of the foliation and deformation processes in this transect is beyond the scope of this study.

#### 3.1. Petrography

Zone I consists of highly deformed and foliated serpentinite that is similar to the mylonitic serpentinite that was studied by Cannaò et al. (2016). Samples of Zone I were collected from both the proximal and distal ends to the contact. Thin section petrography, Raman, SEM, and TGA-DSC analyses revealed nearly monomineralic serpentine (antigorite), in addition to traces of talc, magnetite, and relict chromite (Figure 2a; Figure S3 in Supporting Information S2). These minerals chiefly occur in non-pseudomorphic textures, whereas pseudomorphic mesh and bastite textures after olivine and pyroxene are rare and limited to undeformed serpentinite domains (see Cannaò et al., 2016). Olivine and pyroxene are completely altered to serpentine with minor talc localized near the magnetite. Some accessory magnetite grains show alteration to iron oxy-hydroxide as identified by EPMA. We did not observe any systematic increase in the modal proportions of talc and magnetite toward the contact. Brucite was not detected in any sample using TGA-DSC or Raman spectroscopy (Klein et al., 2020). A subset of serpentinite samples that were collected farthest from the field contact reveal pseudomorphic textures, suggestive of serpentinization under static conditions. Antigorite was identified as the sole serpentine phase based on its characteristic Raman spectrum (Groppo et al., 2006; Petriglieri et al., 2015). Neither chrysotile nor lizardite were found in the samples (Figure S4 in Supporting Information S2).

Zone II is dominated by Ca-amphibole with subordinate chlorite intergrown with euhedral ilmenite. Calcic amphibole occurs as long prismatic grains embedded within a chlorite-rich matrix. Ilmenite is mantled by titanite. Rutile and magnetite are accessory phases in this zone (Figure 2b; Figures S2 and S4 in Supporting Information S2).

Zone III is mainly composed of chlorite, prismatic Ca-amphibole, clinopyroxene, and opaque minerals. Clinopyroxene cores are omphacitic and show an exsolution texture as well as variable replacement by chlorite whereas rims are diopsidic in composition. Rare garnet occurs as anhedral grains within a chlorite matrix and as inclusions in epidote and Ca-amphibole (close to the Zone IV contact, e.g., samples B03 and B04). As in Zone II, ilmenite is mantled by titanite. Rutile is an accessory phase in this zone (Figures 2c–2e; Figures S1 and S3 in Supporting Information S2).

Zone IV is characterized by a range of mineral assemblages that change in composition with distance from the contact. Samples closest to Zone V are characterized by garnet, omphacitic and diopsidic clinopyroxene, Na-Ca amphibole, ilmenite, rutile and titanite, minor albite, white mica, and quartz (Figures 2f–2h). The modal abundances of diopsidic clinopyroxene, epidote, and Ca-amphibole in Zone IV increase toward the contact. Subdomains consist of 1) epidote + diopsidic clinopyroxene, albite, quartz, minor garnet, and localized veinlets of Na-Ca amphibole or 2) abundant garnet, along with minor epidote and Na-amphibole. Samples that are more proximal to the contact are dominated by epidote, diopsidic clinopyroxene, Ca-amphibole, and garnet with minor replacement by chlorite. Garnet contains Na-amphibole, clinopyroxene, white mica, ilmenite and rutile

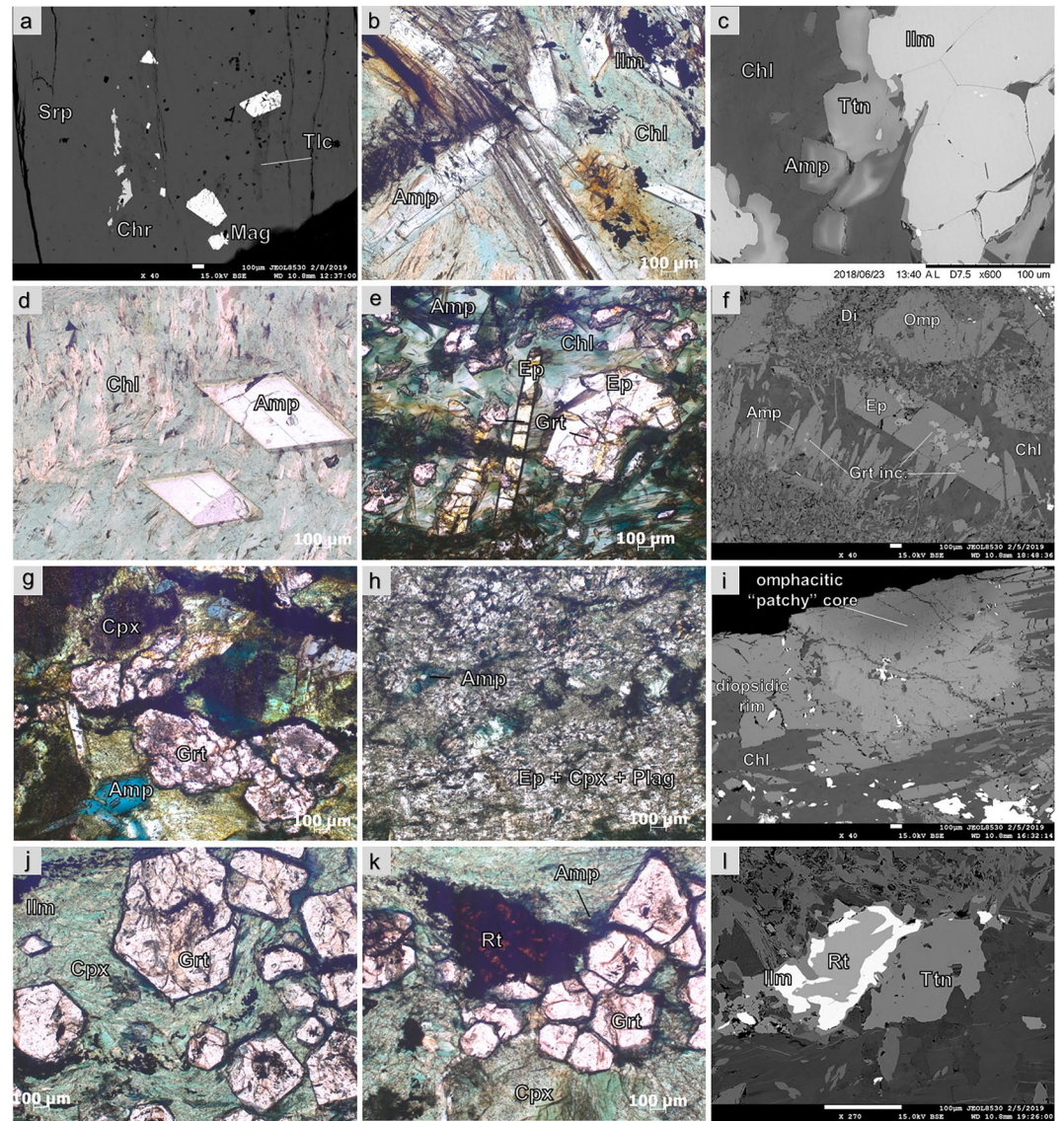


**Figure 2.** Representative photomicrographs and back-scatter electron (BSE) images of the serpentinite-metagabbro transect. (a) antigorite serpentinite with minor talc, magnetite, and chromite grains in Zone I, (b) euhedral, prismatic amphibole schist with chlorite and ilmenite in Zone II, (c) BSE image of ilmenite mantled by titanite coexisting with Ca-amphibole and chlorite typical for Zones II and III, (d) near-monomineralic chlorite schist with Ca-amphibole in Zone III, (e) assemblage of chlorite + Ca amphibole + epidote (with anhedral garnet inclusion) in Zone IV, (f) BSE image of anhedral garnet included within euhedral epidote and Ca amphibole. This feature is common in samples of Zones III and IV. (g) Assemblage of subhedral to euhedral garnet, brown omphacitic clinopyroxene, and bluish Na-Ca amphibole in Zone IV, (h) aggregates of dominantly diopsidic clinopyroxene + epidote + plagioclase with minor Na-Ca amphibole, (i) omphacitic clinopyroxene core showing “patchy” exsolution texture, mantled by diopsidic rim, (j and k) eclogitic metagabbro with euhedral garnet and omphacitic clinopyroxene, rutile, with minor amphibole in Zone V, and (l) BSE image of the assemblage of rutile and ilmenite mantled by titanite in Zone IV and V.

inclusions that were identified either petrographically or using confocal Raman spectroscopy (Figures S2 and S4 in Supporting Information S2). Interlocking grains of ilmenite and rutile that are mantled by titanite are present throughout Zone IV.

Zone V, collected farthest from the field contact, represents the least altered metagabbro and is dominated by garnet, omphacitic clinopyroxene, Na-Ca amphibole, Ti-rich phases (i.e., ilmenite, rutile, titanite), minor diopsidic clinopyroxene, epidote, albite, and accessory sulfide (pyrite) (Figures 2i–2k; Figures S2 and S4 in Supporting Information S2). Similar to Zone IV, the opaque assemblage also shows interlocking grains of ilmenite and



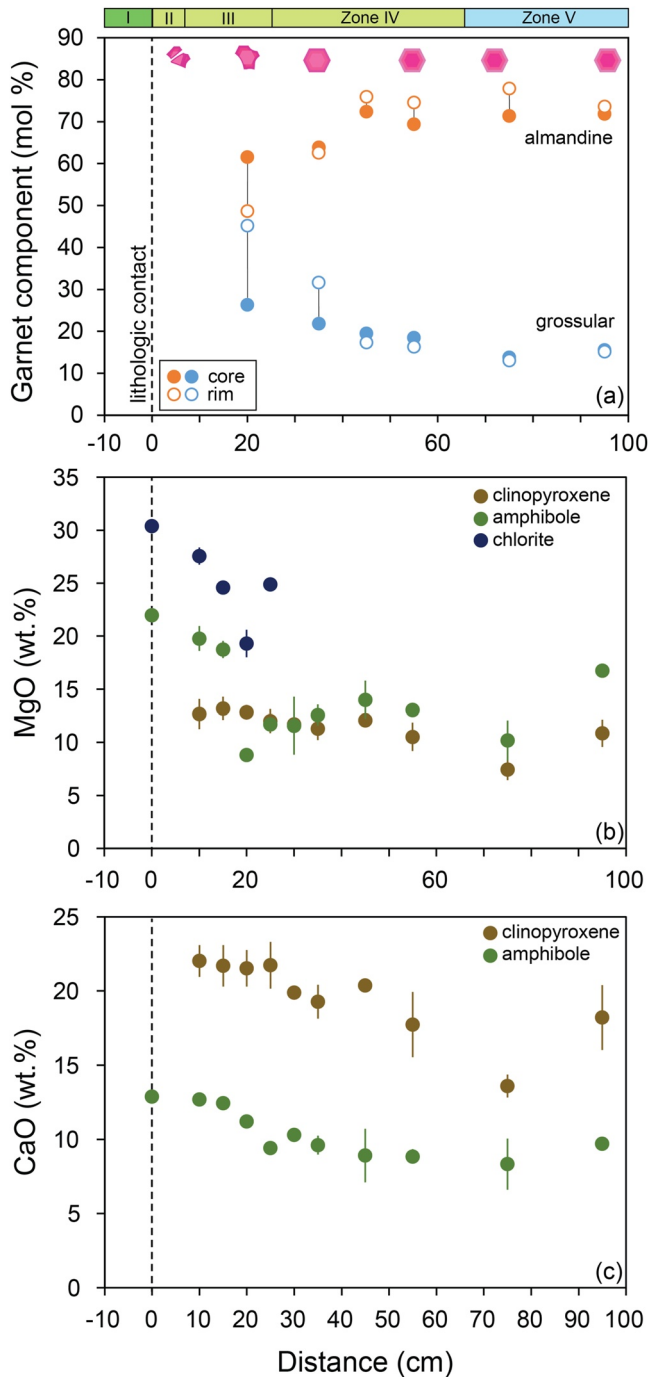


**Figure 3.** Compositional variations of major minerals across the serpentinite-metagabbro transect. (a) core-to-rim variations in almandine and grossular components in garnet (with schematics of their morphology), (b) MgO contents variations (average + 1 SD) in clinopyroxene, amphibole, and chlorite, (c) CaO contents variations (average + 1 SD) in clinopyroxene and amphibole.

rutile that are mantled by titanite (Figure 2l). Garnet contains Na-Ca amphibole, clinopyroxene, epidote and paragonite (inferred to be pseudomorphic after lawsonite; Figure S5 in Supporting Information S2) and rutile inclusions that were identified using confocal Raman spectroscopy. In comparison with Zones III and IV, garnet in samples in Zone V showed the least extensive replacement by chlorite.

### 3.2. Mineral Chemistry Variations

Average major element compositions of the major minerals in each zone are summarized in the supplementary table. Clinopyroxene is found in Zones II to V, and its composition varies systematically, especially in Zones II to IV. The major element compositions of the primary omphacitic clinopyroxene in Zones II-IV are variable, with Mg# [= molar Mg/(Mg + Fe)] ranging from ~0.5 to 0.7, while the secondary diopsidic clinopyroxene mantling the omphacitic clinopyroxene in Zones II and III shows a systematic increase in Mg# (0.72–0.81), along with CaO, MgO, and a decrease in Al<sub>2</sub>O<sub>3</sub> contents, toward the contact (Figure 3b). Omphacitic clinopyroxene cores across the different zones are variably altered to diopsidic compositions (i.e., higher Ca and lower Na contents) and show patchy, μm-scale chlorite alteration (Figure 2i).

Garnet across the different zones displays systematic changes in core-to-rim compositions with distance to the lithologic contact (Figure 4, Figure S6 in Supporting Information S2). Euhedral to subhedral garnet (~1 mm average diameter in B09 and B10) in Zone V displays systematic decrease in MnO contents from core (>5 wt. %) to rim (<0.5 wt. %) at relatively constant and low CaO contents (≤8 wt. %). Garnet in sample B08 (~0.5 mm average diameter, Zone IV) shows compositional characteristics similar to garnet in Zone V with concentric Mn-growth zoning (i.e., decreasing Mn from core to rim) and low and constant CaO contents (Figures 4e and 4f). Garnet in sample B07 (~0.5 mm average diameter, Zone IV) also displays the same Mn-growth zoning and fairly low CaO contents. However, the garnet rims in sample B07 display slight enrichment in CaO contents (>8 wt. %) relative to more distal samples (Figures 4g and 4h). The more proximal garnet in B06 (~0.4 mm average diameter, Zone IV) displays similar core-to-rim MnO zoning to the more distal samples but with distinctly opposite core-to-rim CaO trends. In particular, the cores of garnet in B06 have CaO contents similar to the garnet from more distal samples (~8 wt. %) but their rims systematically increase to up to ~12 wt. % CaO. Garnet in Zones IV and V has decreasing almandine contents and increasing pyrope contents from core (average of Alm<sub>72</sub>Prp<sub>3</sub>Sps<sub>10</sub>Gr<sub>16</sub>) to rim (average of Alm<sub>74</sub>Prp<sub>10</sub>Sps<sub>1</sub>Gr<sub>15</sub>). Samples in Zone IV that are more proximal to the contact have garnet that, on average, have lower almandine and higher grossular contents than more distal ones (Figure 3a). In addition, the core-to-rim variations in these proximal garnets show increasing grossular and decreasing spessartine contents from core (Alm<sub>64</sub>Prp<sub>2</sub>Sps<sub>12</sub>Gr<sub>22</sub>) to rim (Alm<sub>63</sub>Prp<sub>3</sub>Sps<sub>3</sub>Gr<sub>32</sub>). Garnet in samples more proximal to the contact, that is, Zone III, are anhedral and pervasively resorbed and replaced by chlorite. This makes it difficult to determine whether the measured grain represents the core or rim. For this purpose, we assumed that the rim would have the highest CaO content following the observed systematic trend from the closest garnets in Zone IV (B06 and B07). Garnets in Zone III are grossular-rich (Alm<sub>62</sub>Prp<sub>8</sub>Sps<sub>4</sub>Gr<sub>26</sub>

core to Alm<sub>49</sub>Prp<sub>3</sub>Sps<sub>3</sub>Gr<sub>45</sub> rim), with CaO content exceeding the core-to-rim range of garnets from the more distal Zones IV and V. For instance, the compositions of anhedral garnet included within euhedral epidote (Alm<sub>49</sub>Prp<sub>4</sub>Sps<sub>4</sub>Gr<sub>43</sub>) and calcic amphibole (Alm<sub>50</sub>Prp<sub>4</sub>Sps<sub>4</sub>Gr<sub>42</sub>) are grossular-rich. The MnO contents of Zone



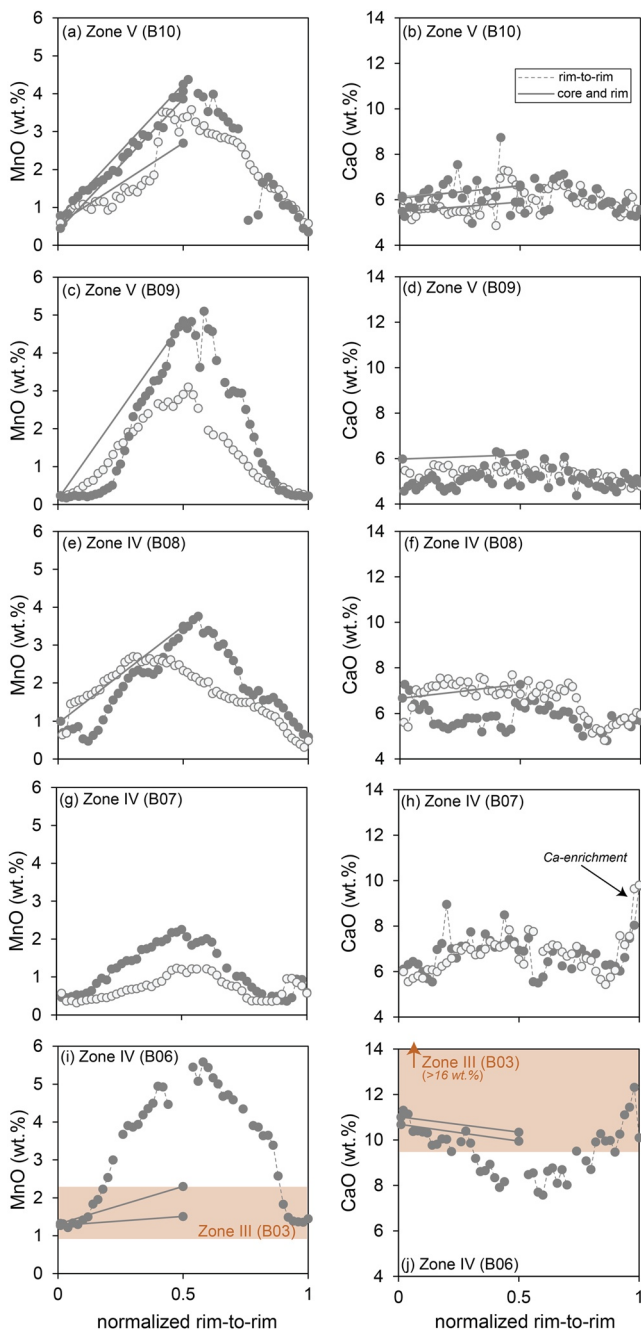


**Figure 4.** Representative rim-to-rim compositional variations of garnet from different zones. Variations in (a) MnO and (b) CaO contents (wt. %) are measured by electron microprobe analysis. Different symbols represent different analyzed garnet grains for each zone. The rim-to-rim distance of garnet are normalized for comparison. Representative photomicrographs of measured grains are provided in the supplementary. Due to the difficulty in determining the core and rim of anhedral garnets in Zone III, we plotted the full range of measured composition instead.

III garnets remain within range of garnet compositions from Zones IV and V, with MnO contents plotting closer to the rim compositions of garnets from Zones IV and V (Figures 4i and 4j).

Amphiboles show a wide range of compositions, ranging from sodic to calcic. The MgO and CaO contents of amphiboles generally increase toward the contact. Following the classification of Hawthorne et al. (2012), Zones V and IV contain a wide variety of amphiboles belonging to the Na-Ca group (e.g., winchite, ferri-winchite, barroisite, and katophorite) and the calcic group (e.g., pargasite, actinolite, magnesio-ferri-hornblende, and magnesio-hornblende). Representative core-to-rim compositions of a subset show Na-Ca amphibole (winchite, katophorite) mantled by Ca-rich amphibole (mainly pargasite) in these zones. Zones II and III, which are the closest to the field contact, show less variability in composition compared to Zones IV and V. These zones contain dominantly Ca-rich amphibole, such as hastingsite, actinolite, and tremolite (Figure 3c).

The composition of chlorite (clinocllore) in Zones II and III shows a systematic increase in Mg and Si contents toward the contact (Figure 3b). The Mg# varies from 0.60 to 0.86, with higher values toward the contact. Such compositional variations reflect the combined Fe-Mg exchange between the Mg-endmember clinocllore and the Fe-endmember daphnite, and Tschermak's substitution between daphnite, clinocllore and amesite.

Epidote comprises a dominant fraction of the mineral assemblage in Zone IV. Its composition varies within Zone IV, with generally higher Si (2.98–3.01 atoms per formula unit or a.p.f.u.) for samples farther from the contact to lower Si (2.91–2.95 a.p.f.u.) in samples closer to the contact. The calculated Fe (III) contents show a systematic increase toward the contact, from 0.20 to 0.89 a.p.f.u.

Antigorite is chemically homogenous in Zone I (34.1 wt. % MgO, 41.5 wt. % SiO<sub>2</sub>, 8.6–8.8 wt. % FeO\*, ~2.0 wt. % Al<sub>2</sub>O<sub>3</sub>), with a Mg# of 0.87 and has ~13 wt. % of structurally-bound water. Talc in Zone I also shows a homogenous composition (28.8 wt. % MgO, ~62.0 wt. % SiO<sub>2</sub>, 2.5–2.7 wt. % FeO), with Mg# of 0.95 and has ~6 wt. % of structurally bound water.

Albite of near endmember composition is a minor phase and is generally found with epidote and diopsidic clinopyroxene in Zone IV. Ilmenite in Zones II and III shows variations in composition (49–51 wt. % TiO<sub>2</sub>, 41.5–47.5 wt. % FeO, 0.4–1.7 wt. % MgO), with notable increases in Mg and decreases in Mn contents from Zone III to II. Titanite in Zones II and III shows a homogenous and near-stoichiometric composition (37–39 wt. % TiO<sub>2</sub>, ~30 wt. % SiO<sub>2</sub>, and ~28 wt. % CaO). Accessory phases such as apatite and pyrite are observed in different zones but their compositions are not examined in this study.

### 3.3. Bulk-Rock Major Element Compositional Variation

Systematic chemical changes are observed across the serpentinite-metagabbro transect (Figure 5). On a volatile-free basis, the MgO concentration is highest in serpentinite (Zone I) and gradually decreases toward Zone V. The CaO concentration is lowest in the serpentinite and highest in the metagabbro of Zone IV, but decreases toward Zone V. The concentration of SiO<sub>2</sub> shows

limited variation in Zones I, IV and V but is lower in III, except for one sample in Zone II. The concentration of Al<sub>2</sub>O<sub>3</sub> is mainly elevated in Zone III relative to the adjacent zones. The loss on ignition (LOI; taken as bulk H<sub>2</sub>O) and MgO/SiO<sub>2</sub> show similar enrichment and depletion trends, which reflects the relative abundance of

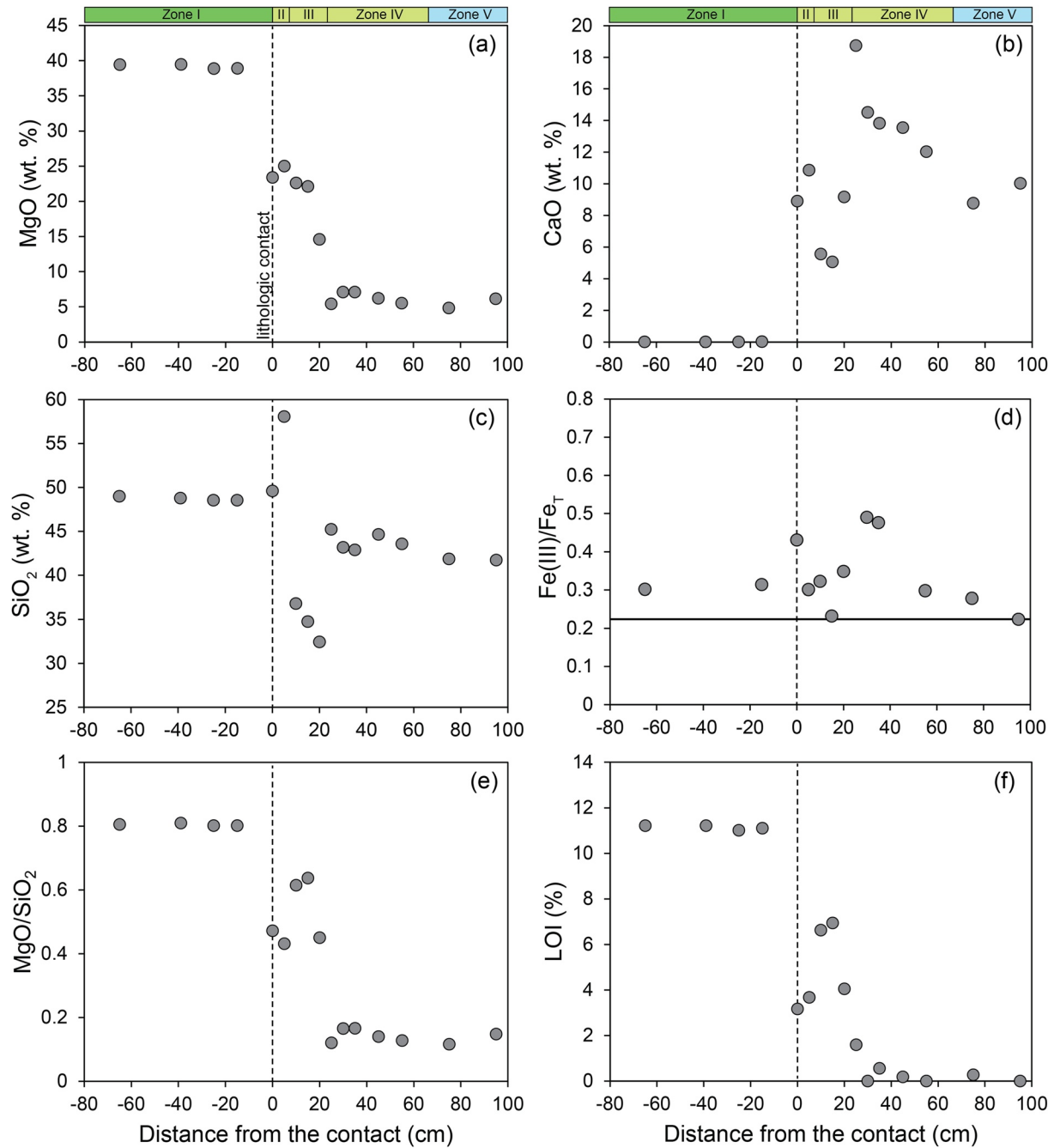


**Figure 5.** Bulk-rock major element concentrations (on a volatile-free basis), (a) MgO, (b) CaO, (c) SiO<sub>2</sub>, (d) Fe(III)/Fe<sub>T</sub>, (e) MgO/SiO<sub>2</sub>, and (f) loss on ignition (LOI) across the serpentinite-metagabbro transect.

Ca-amphibole and chlorite in Zones II and III. The bulk-rock Fe(III)/Fe<sub>T</sub> display elevated ratios in Zone II-IV relative to V, with highest values in IV (Figure 5d). The modal mineralogy and major element compositions (and associated modal mineralogy) of the two samples in Zone V are generally similar, except for differences in Al<sub>2</sub>O<sub>3</sub>.

### 3.4. Bulk-Rock Trace Element Compositional and Sr Isotopic Variation

The rare earth element (REE) concentrations show systematic across-transect trends and a decoupling between light (L-) and heavy (H-) REE (Figure 6a). The LREE concentrations are lowest in serpentinite and are generally elevated in metagabbro in Zones II to V, reaching their highest concentrations in Zone IV. Enrichments in

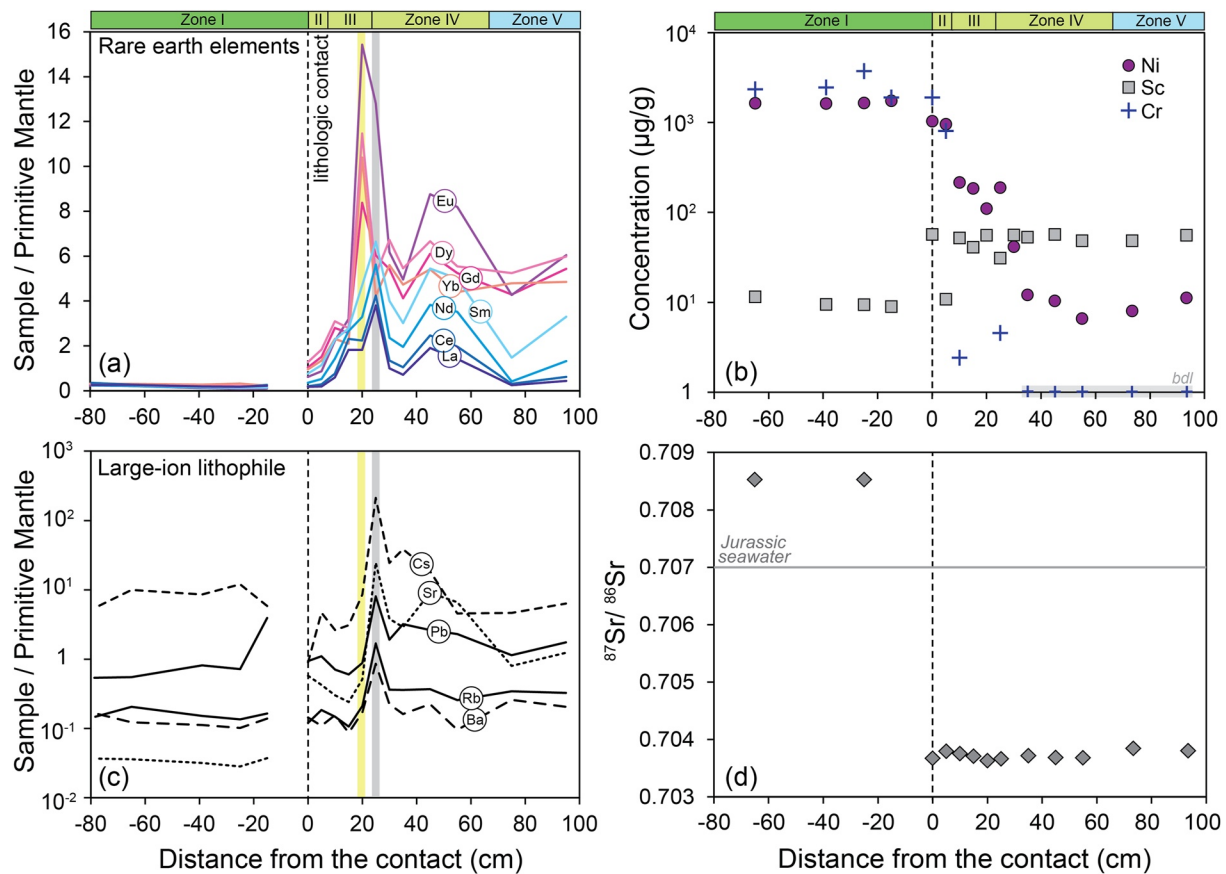


**Figure 6.** Bulk-rock trace-element concentrations normalized to primitive mantle (McDonough & Sun, 1995) and  $^{87}\text{Sr}/^{86}\text{Sr}$  ratios across the serpentinite-metagabbro transect. (a) Rare earth element (REE), (b) transition element (Ni, Cr, and Sc), and (c) large-ion lithophile element (LILE; Cs, Rb, Ba, Sr, Pb), and (d) bulk-rock  $^{87}\text{Sr}/^{86}\text{Sr}$  isotope ratios of the studied samples and Jurassic seawater from Jones et al. (1994). In (a and c), the yellow bar marks the location of peak enrichment for LREE and fluid-mobile LIL elements while the Gy bar marks the location of peak enrichment for HREE.

fluid-mobile elements (e.g., Cs, Sr, Pb, Rb, Ba) are also observed in the samples with the highest LREE enrichments in Zone IV (Figure 6c). On the other hand, HREE concentrations are lowest in Zone I, but only gradually increase to roughly steady concentrations from Zones II to V. The peak enrichments in HREE are observed in Zone III, adjacent to the LREE-enriched Zone IV samples. Nickel and Cr show a gradual decrease from high concentrations in Zone I to Zones IV and V while Sc shows a step-wise function separating Zone I from Zones II-V (Figure 6b).

Primitive Mantle-normalized REE patterns of serpentinite vary little among the analyzed samples, and display a slight increase from La to Lu. In comparison, metagabbro in Zone II show similar primitive mantle-normalized abundances for LREE and Th, but with higher Sr and HREE relative to serpentinite. Metagabbro of Zone III is more enriched in REE, but is slightly depleted in fluid-mobile elements compared to Zone II. The metagabbros of Zone IV display the highest concentrations in LREE, Sr, and Pb among the measured samples. Metagabbros of Zone V have similar flat HREE patterns as in Zone IV, but are strongly depleted in LREE (relative to HREE), Sr, and Pb (Figure 7). The  $(\text{La}/\text{Sm})_N$  ratio (N, normalized to Primitive Mantle) of serpentinite systematically increases toward the contact. Similarly, the  $(\text{La}/\text{Sm})_N$  increases toward the contact from Zone V to Zone II within the metagabbro side. Both metagabbro samples in Zone II have lower values of  $(\text{La}/\text{Sm})_N$  than the adjacent zones (Figure S7 in Supporting Information S2). The two samples from Zone V display similar primitive mantle-normalized trace element patterns expect for Zr, Hf, Nb, and Ta.

The age-corrected (40 Ma from Starr et al., 2020) bulk-rock  $^{87}\text{Sr}/^{86}\text{Sr}$  isotope ratio of serpentinite is  $0.7083 \pm 0.0004$  (average  $\pm 1$  SD). Metagabbro in Zones II to V displays a constant  $^{87}\text{Sr}/^{86}\text{Sr}$  isotope ratio of  $0.7037 \pm 0.0001$ . This distribution reflects a step-function from the more radiogenic Sr in the serpentinite of



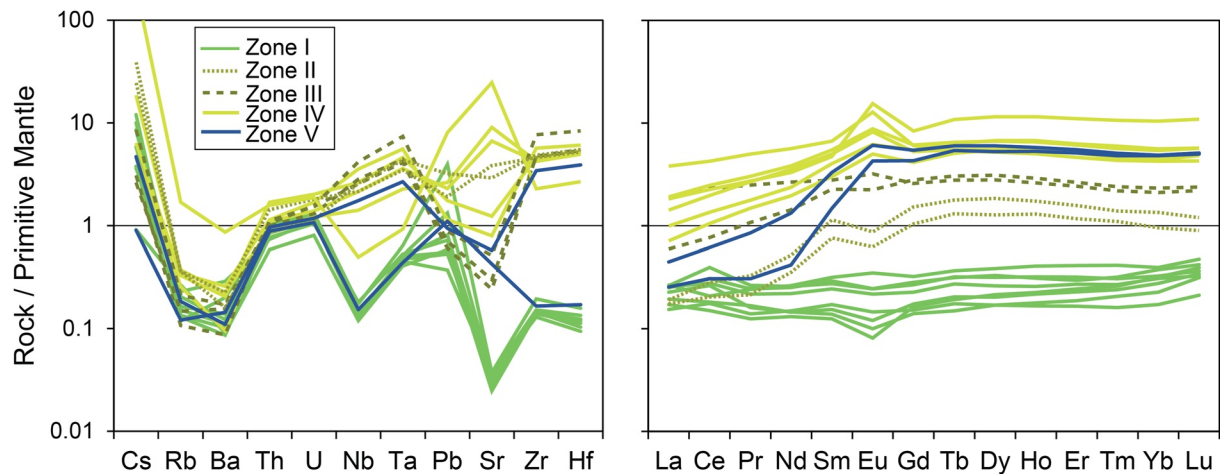


**Figure 7.** Primitive Mantle-normalized trace-element systematics of the Voltri serpentinite-metagabbro transect. Primitive mantle values are taken from McDonough and Sun (1995).

Zone I to the less radiogenic Sr in Zones II to V (Figure 6d). The bulk-rock Sr concentration mirrors the bulk-rock CaO trend, with the highest values in Zone IV, the lowest in Zone I, and intermediate and roughly similar values across Zones II, III, and V.

### 3.5. Density and Magnetic Susceptibility

Variations in the mineralogy and bulk-rock chemistry are reflected in their bulk density and magnetic susceptibility. Across-transect variations between the serpentinite and metagabbro (Figure 1c) show that the density systematically decreases from the distal eclogite ( $\rho = 3.6 \text{ g/cm}^3$  in Zone V) toward the distal serpentinite ( $\rho = 2.6 \text{ g/cm}^3$  in Zone I) through the reaction zones II, III and IV, with values intermediate between Zones I and V. Zone IV has an average bulk density of  $\sim 3.5 \text{ g/cm}^3$  while Zones II and III have densities of  $3.0 \text{ g/cm}^3$ . The magnetic susceptibilities are low and near-constant for metagabbro of Zones IV and V ( $15.3\text{--}42.8 \text{ SI} \times 10^{-5}$ ) relative to high values in Zone III ( $238\text{--}375 \text{ SI} \times 10^{-5}$ ). Serpentinite of Zone I and metagabbro of Zone II have low and near-constant magnetic susceptibility values ( $11.0\text{--}134 \text{ SI} \times 10^{-5}$ ) comparable to Zones IV and V. For comparison, the bulk magnetic susceptibility reported for oceanic serpentinites can reach up to  $12 \times 10^{-2} \text{ SI}$  (Klein et al., 2014).

### 3.6. Pressure-Temperature Constraints

Thermodynamic phase equilibria were calculated in order to constrain the metamorphic  $P$ - $T$  evolution of the Voltri metagabbro and the relative timing of mass transfer. Pseudosection modeling of the whole rock composition, coupled with garnet crystal core chemical isopleths, allows for the calculation of the  $P$ - $T$  conditions of garnet growth initiation while pseudosection modeling of the matrix (fractionated whole rock) compositions, coupled with garnet crystal rim chemical isopleths, allows for the calculation of the peak to post-peak  $P$ - $T$  conditions. Moreover, pseudosection modeling of the stable mineral assemblage using the whole rock compositions of the most reacted samples allows for calculation of the  $P$ - $T$  conditions during the final stages of element mass transfer along the sample transect. In these samples, there are no porphyroblastic phases, like garnet, that would significantly fractionate elements, thereby changing the effective whole rock compositions. For all pseudosection results presented below, uncertainties in pressure and temperature estimates are regarded to be on the order of  $\pm 0.1 \text{ GPa}$  and  $\pm 40^\circ\text{C}$  (Palin et al., 2016).

The results of the phase equilibria modeling for sample B10 (Zone V) are shown in Figure 8 and the results of modeling for representative bulk compositions of Zones II-IV are shown in Figure 9. Garnet crystal core growth is calculated to have occurred in the mineral assemblage field garnet + omphacite + chlorite + lawsonite + rutile ( $\pm$ quartz). This calculated assemblage is broadly consistent with the petrographic observations of garnet cores containing inclusions of omphacite, lawsonite pseudomorphs and rutile. Garnet crystal rim growth is calculated to have occurred in the mineral assemblage field garnet + omphacite + amphibole + chlorite + rutile ( $\pm$ talc).

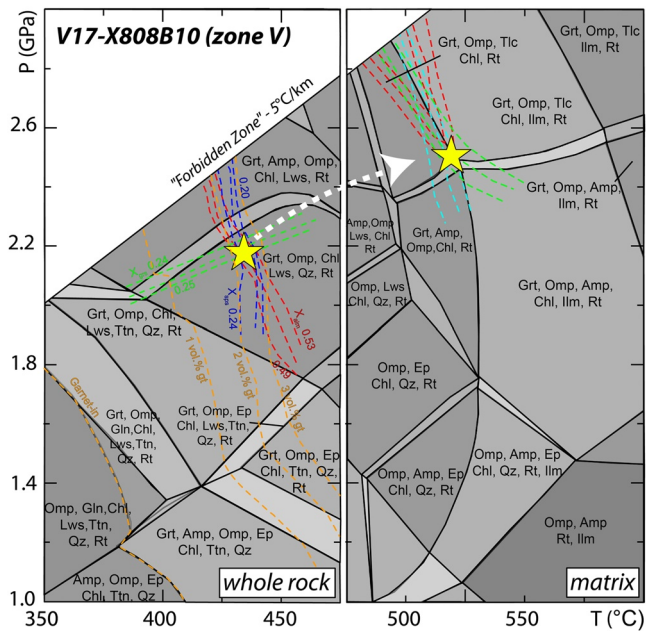


**Figure 8.** Pressure and temperature constraints on the initiation and termination of garnet growth determined for the MnNCFMASHTO chemical system. Pseudosection modeling for the whole rock composition (left panel) and matrix compositions (excluding garnet; right panel) are performed for the most distal eclogitic metagabbro (Zone V). Garnet chemical isopleths corresponding to observed core and rim garnet chemistry are plotted on whole-rock and matrix pseudosections, respectively (almandine = red, grossular = green, spessartine = blue). Garnet-in conditions and garnet modal abundances (vol. %; orange dashed lines) are also included. The intersection of the garnet core chemical isopleths constrains the P-T range for the initiation of garnet growth while the intersection of the garnet rim chemical isopleths constrains the P-T range at the termination of garnet growth.

This is consistent with the observations of Na-amphibole inclusions within garnet and Na-Ca amphibole and chlorite in the matrix. While talc is calculated to have been stable during the growth of garnet rims, it is neither found as inclusions in garnet nor as a matrix phase. However, the calculated abundance of talc is  $<0.1$  vol. %, and is thus deemed negligible. Calculated  $P$ - $T$  conditions for initial growth of garnet in sample B10, constrained by garnet core isopleth intersections and agreement between observed inclusion assemblages and calculated assemblages, are  $\sim 2.2$  GPa and  $430^\circ\text{C}$ . Calculated  $P$ - $T$  conditions for garnet rim growth are  $\sim 2.5$  GPa and  $\sim 520^\circ\text{C}$  (Figure 8). This is further defined as the peak  $P$ - $T$  condition for the samples of interest.

Garnet core growth for sample B06 (Zone IV) is calculated to have occurred in the mineral field assemblage garnet + omphacite + chlorite + lawsonite + ilmenite + rutile ( $\pm$ talc). This is broadly consistent with the observed garnet core inclusions, including omphacite, epidote + paragonite (inferred to be pseudomorphic after lawsonite), ilmenite and rutile. As above, the calculated abundance of talc was deemed negligible. Garnet rim growth in sample B06 is calculated to have occurred in the mineral field assemblage garnet + omphacite + chlorite + lawsonite + epidote + ilmenite + rutile ( $\pm$ amphibole). This is consistent with observed garnet inclusions of omphacite, Na-amphibole, lawsonite pseudomorphs (epidote + white mica), ilmenite and rutile. Calculated  $P$ - $T$  conditions for initial growth of garnet in sample B06 are  $\sim 2.4$  GPa and  $470^\circ\text{C}$ . Calculated  $P$ - $T$  conditions for garnet rim growth are  $\sim 1.8$  GPa and  $\sim 500^\circ\text{C}$  (Figure 9d). Modeling of the stable mineral assemblage using the matrix composition for sample B06 highlights partial re-equilibration at lower pressure. This is consistent with the presence of titanite rims around ilmenite and rutile, with a calculated maximum pressure (for the mineral assemblage omphacite + amphibole + chlorite + epidote + ilmenite + titanite) of  $\sim 0.8$ – $0.9$  GPa at  $\sim 475^\circ\text{C}$  (Figure 9e). With this estimate, we assume relatively isothermal decompression after attainment of peak  $P$ - $T$  conditions, consistent with previous constraints (Malatesta et al., 2012a). In this portion of the phase diagram, the titanite-in reaction line has a negative  $dP/dT$ , and thus any early cooling upon decompression would result in traversing the reaction line at higher

pressure. It should be noted, however, that the bulk rock  $\text{Fe(III)/Fe}_T$  exerts a significant control on the stability of Ti-bearing phases (Diener & Powell, 2010), and thus the maximum pressure at which titanite is stable may vary. For both samples B10 (Zone V) and B06 (Zone IV), (a) the intersections of the garnet core compositional isopleths are situated up to  $100^\circ\text{C}$  and from 0.4 to 1.0 GPa above the initial stability of garnet (see Figures 8 and 9d), and (b) the estimated volume abundance of garnet at these points is  $\sim 2$  vol. % and  $\sim 5$  vol. %, respectively. The implications of these calculations will be discussed below (see Section 4.4). However, it should be noted that model observations such as these have been attributed to either kinetic limitations to mineral growth (Carlson et al., 2015) or inaccuracies in bulk rock composition.

Phase equilibria modeling of sample B01 (Zone III), combined with a comparison of observed and calculated mineral assemblages, allows for the calculation of the  $P$ - $T$  conditions during the final stages of metamorphism. This is motivated by the clear textural relationship of garnet replacement by chlorite which suggest that B01 last equilibrated at  $P$ - $T$  conditions post eclogite-facies metamorphism. At the peak  $P$ - $T$  conditions of  $\sim 2.5$  GPa and  $\sim 520^\circ\text{C}$ , the calculated stable mineral assemblage is clinopyroxene + chlorite + talc + ilmenite + rutile. Comparisons between petrographic observations and calculated phase equilibria are suggestive of partial re-equilibration during decompression. These include (a) the absence of talc in the observed stable mineral assemblage, (b) blueschist-facies overprinting represented by the growth of Na-Ca amphibole at the expense of clinopyroxene at pressures below  $\sim 2.3$  GPa (note the appearance of cpx grains in Figure 2f), and (c) the presence of titanite mantling ilmenite throughout sample B01 (Figure 2c). The observed mineral assemblage clinopyroxene + amphibole + chlorite + ilmenite + titanite is calculated to occur at a maximum pressure of  $\sim 1.6$  GPa at  $500^\circ\text{C}$ . The appearance of magnetite, observed petrographically to be a late-stage phase, is calculated to be stable at pressures

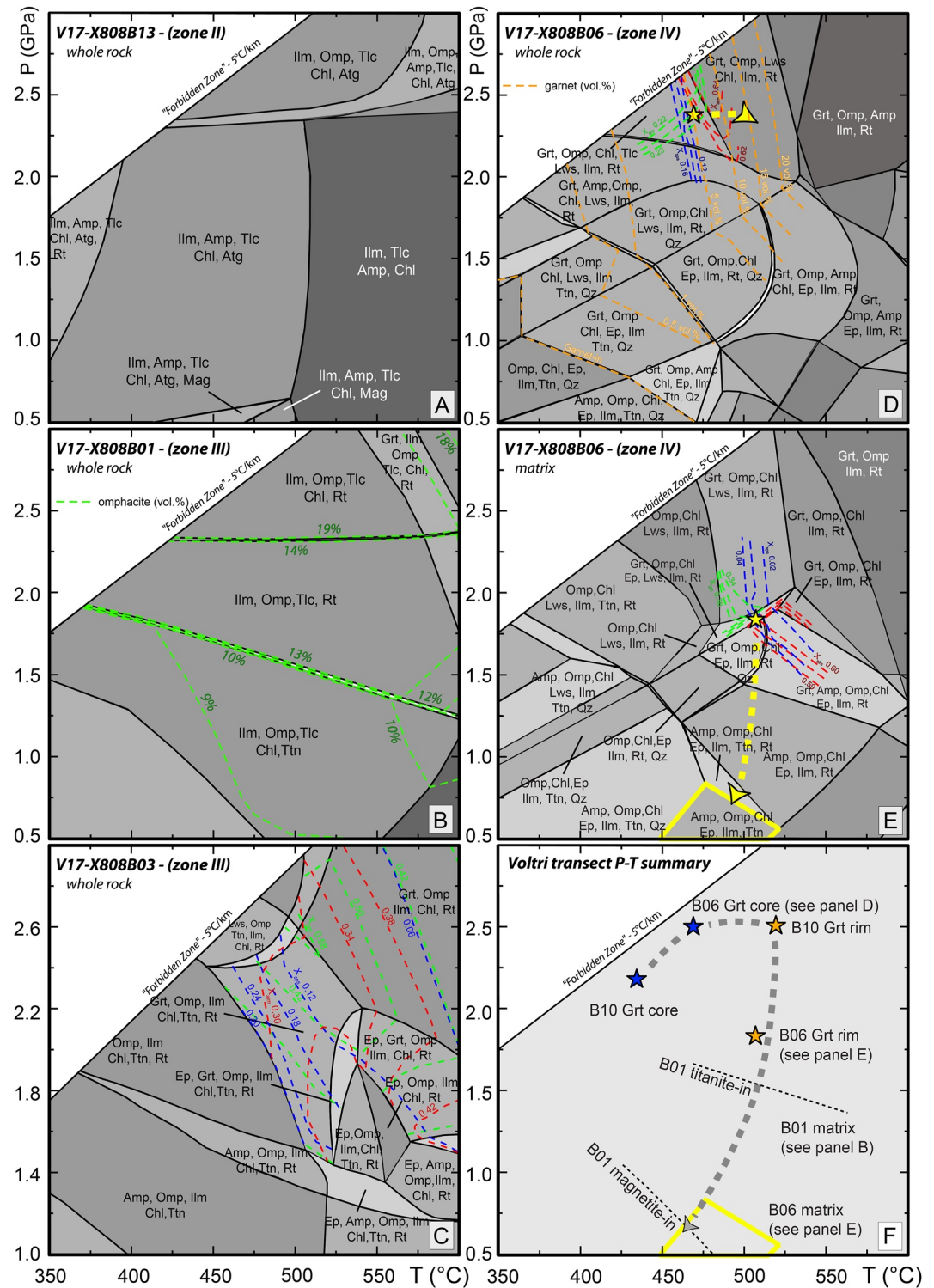


**Figure 9.** Pseudosection modeling for representative samples in each metasomatic reaction zone in the MnNCFMASHTO chemical system. (a) Whole-rock Zone II, (b) whole-rock Zone III, (c) whole-rock Zone III with predicted garnet chemical isopleths (almandine = red, grossular = green, spessartine = blue) calculated at peak P-T conditions as constrained by Zone V, (d and e) whole-rock and matrix, Zone IV, and (f) P-T summary for the entire metasomatic reaction zones. Garnet-in conditions and garnet modal abundances (vol. %; orange dashed lines) are also included in (d) while omphacite modal abundances (vol. %; green dashed lines) are included in (b). See text for details. Mineral abbreviations are from Whitney and Evans (2010).



below  $\sim 0.7$  GPa at  $450\text{--}475^\circ\text{C}$  (Figure 8b). This is interpreted to record final equilibration associated with the early stages of exhumation and thus may help further constrain the retrograde metamorphic pressure-temperature history.

Sample B13 in Zone II represents one of the most strongly metasomatized bulk compositions along the transect. The calculated stable mineral assemblage at the peak  $P$ - $T$  conditions is clinopyroxene + chlorite + talc + ilmenite ( $\pm$ antigorite). Similar to sample B01 in Zone III, Ca-amphibole is calculated to be stable and form at the expense of clinopyroxene at pressures below  $\sim 2.3$  GPa. Few other constraints on  $P$ - $T$  conditions can be made from these lithologies. As mentioned earlier, the presence of magnetite as an accessory phase is calculated to be stable at pressures below  $\sim 0.6$  GPa and temperatures below  $\sim 500^\circ\text{C}$  (Figure 9a).

In an attempt to calculate the  $P$ - $T$  conditions of garnet growth in Zone III that experienced significant Ca enrichment and to identify the relative timing of this enrichment, the bulk composition for sample B03 was modeled (Figure 9c). Calculated garnet chemical isopleths were compared to measured garnet core and rim compositions. The calculated stable mineral assemblage at the peak  $P$ - $T$  conditions is garnet + clinopyroxene + chlorite + ilmenite + rutile. The calculated garnet composition at the peak  $P$ - $T$  condition is  $\text{Alm}_{32}\text{Prp}_{05}\text{Sps}_{07}\text{Grs}_{56}$ . As noted earlier the observed compositions for garnet crystal core and rim in sample B03 are  $\text{Alm}_{62}\text{Prp}_8\text{Sps}_4\text{Grs}_{26}$  and  $\text{Alm}_{49}\text{Prp}_3\text{Sps}_3\text{Grs}_{45}$ , respectively. The calculated garnet composition at the peak  $P$ - $T$  condition provides a composition that is significantly more grossular-rich (and almandine-poor) than observed. The significance of this discrepancy for the timing of mass transfer will be discussed in Section 4.4.

To summarize the results from phase equilibria modeling, Zones IV and V are inferred to record the prograde to peak to post-peak  $P$ - $T$  conditions for the metagabbro-serpentinite contact studied here. The inferred peak  $P$ - $T$  condition for this locality is  $\sim 2.5$  GPa and  $520^\circ\text{C}$  (Figure 9f). The similarity in the  $P$ - $T$  path recorded in Zones IV and V suggests that the bulk compositions for these zones were established prior to peak metamorphic conditions. This is further supported by textural equilibrium in Zones IV and V (Figures 2g and 2j; Figure S2 in Supporting Information S2). The peak  $P$ - $T$  constraints are also taken as a maximum  $P$ - $T$  constraint for the formation of Zones II and III because of the clear petrographic relation of garnet being replaced by chlorite in these zones. Pervasive, although minor, blueschist- and greenschist-facies overprinting has already been inferred for lithologies across the Voltri Ophiolite (Starr et al., 2020). This is also evident in the studied metagabbro-serpentinite contact by localized partial re-equilibration of Zones II, III and IV. All samples from zones II to V contain Ti-bearing phases (i.e., rutile and ilmenite) that are mantled by titanite. Therefore, the  $P$ - $T$  condition of formation of these titanite rims serve as a lower limit for the formation of Zones II and III (Figure 2l). Based on these and previous constraints, we infer a clockwise  $P$ - $T$  path, that exhibits a phase of relatively isothermal decompression at  $\sim 500\text{--}520^\circ\text{C}$  from the peak pressure of  $\sim 2.5$  GPa down to  $\sim 1.0$  GPa (Figure 9f). Lastly, these results are consistent with previous regional thermobarometric constraints for the Voltri Massif (Malatesta et al., 2012a; Smye et al., 2021; Starr et al., 2020).

### 3.7. Reaction-Path Modeling

Reaction-path models were calculated to further constrain metasomatic reactions between serpentinite and metagabbro. In our models, we first calculated the aqueous fluid composition and equilibrium speciation controlled by a serpentinite assemblage composed of antigorite + clinopyroxene (diopside) + magnetite  $\pm$  brucite, and tracked their activities as a function of temperature and pressure. We did not model serpentinization of mantle peridotite at subduction zone conditions. Rather, we calculated the composition of an aqueous fluid coexisting with, and buffered by a serpentinite assemblage. We present the speciation of Mg, Si, and Ca, and their activities from  $300$  to  $550^\circ\text{C}$  and  $1.0\text{--}2.5$  GPa (Figure 10). Note that for the sake of clarity, we only report the two most abundant species of each of these elements. However, we do not report the predicted activities for Fe and Al species which are all below  $10^{-5}$ . Over the range of  $P$ - $T$  conditions determined for the studied samples,  $\text{Mg}(\text{OH})_{2(aq)}$  is predicted to be the dominant species followed by  $\text{H}_4\text{SiO}_{4(aq)}$  (i.e.,  $\text{SiO}_{2(aq)}$ ) and  $\text{H}_3\text{SiO}_4^-$  in the fluid. The predicted activity of  $\text{Mg}(\text{OH})_{2(aq)}$  increases with increasing temperature but generally decreases with increasing pressure. Conversely, the activities of all Si species increase with increasing pressure while Ca species remain broadly unchanged. The activities of Ca species are predicted to remain fairly constant as temperature increases and are three orders of magnitude lower than the activity of  $\text{Mg}(\text{OH})_{2(aq)}$ . Notably, the activities of Mg

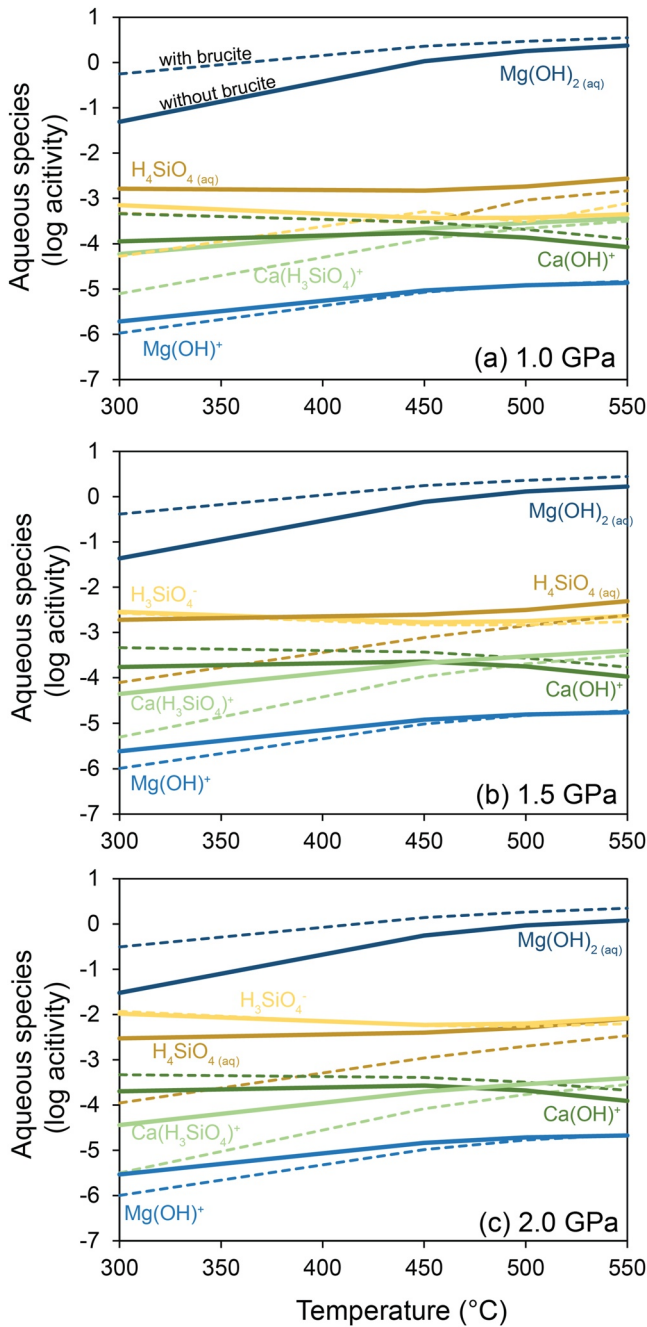


**Figure 10.** Predicted speciation and activities of Mg, Si, and Ca in equilibrium with serpentinite (i.e., antigorite + clinopyroxene + magnetite ± brucite), and their evolution with temperature (300–550°C) and pressure (1.0–2.0 GPa) (panels a to c).

species are higher while the activities of Si species are lower in fluids coexisting with a brucite-bearing serpentinite compared to a brucite-free serpentinite at the same  $P$ - $T$  conditions.

We then modeled the isobaric and isothermal metasomatism of gabbro by allowing it to react with a fluid that was in equilibrium with serpentinite (Figure 11). We used the  $P$ - $T$  constraints derived from the pseudosection modeling (Section 3.6) and predicted the fluid composition in equilibrium with a brucite-free serpentinite consistent with petrographic observations. The model procedure was to titrate gabbro in small increments into the fluid that previously equilibrated with serpentinite. The reaction path therefore portrays a system that is initially fluid-dominated but that becomes increasingly rock-dominated as more metagabbro is added. One could envision that this model represents local fluid–rock equilibria as fluid travels from serpentinite into gabbro (Figure 11). The possibly large porosity and permeability contrasts between serpentinite and metagabbro are likely to promote spatial variations in fluid fluxes and fluid-to-rock ratios between metagabbro block interior and surrounding serpentinite, as suggested by numerical models (Ague, 2007). This modeling approach circumvents some potential complexities in investigating subduction zone processes. For instance, our approach can simulate the reaction between a serpentinite-buffered fluid and adjacent metagabbro regardless of whether the release of fluids during subduction is episodic or continuous and whether the fluids are derived locally (i.e., from the breakdown of brucite in serpentinite) or externally (i.e., other subducted hydrated lithologies) as long as the fluids are last equilibrated with serpentinite before reacting with the metagabbro. In this study, we calculated two model series, one with gabbro and another one with eclogite as reactants. The gabbro-fluid model explores the possibility that fluid-mediated mass transfer occurred during prograde to peak metamorphism, modifying the bulk composition of each zone, before reaching peak eclogite-facies metamorphism and post-peak retrograde conditions. In comparison, the eclogite-fluid model explores the possibility that the fluid-mediated mass transfer only occurred at post-peak eclogite-facies and retrograde conditions. Importantly, only the model that used gabbro predicts mineral assemblages that are observed in the reaction zones (Figure 11). The model results for reaction with eclogite are presented in the supplement. The serpentinite-equilibrated fluid, before reaction with gabbro (indicated at the lowest  $\xi$  value, i.e., maximum  $f/r$  ratio), is predicted to be dominated by dissolved Mg in all models, with subordinate dissolved Si, Ca, Al, and Fe. The models generally show similar mineral assemblages between 450 and 550°C. With decreasing  $f/r$  ratios over this temperature range, the predicted sequence of minerals formed is antigorite + clinopyroxene → serpentine + clinopyroxene + chlorite → chlorite + clinopyroxene ± tremolite → garnet + chlorite + clinopyroxene → epidote + chlorite + clinopyroxene ± garnet → chlorite + clinopyroxene + epidote + paragonite ± plagioclase ± quartz. Magnetite is predicted to form in all simulations. The composition and oxygen fugacity ( $fO_2$ ) of the coexisting fluid vary with increasing  $f/r$ . Over a range of modeled  $P$ - $T$  conditions, the concentration of dissolved Mg decreases, while dissolved Si increases with decreasing  $f/r$  ratio. The dissolved Al concentration is most

elevated at intermediate  $f/r$  ratios and is mirrored by depletions in Ca and Fe. The predicted  $fO_2$  at intermediate  $f/r$  ratios is decreased relative to that of the most rock-buffered system ( $f/r = 10$ ) (Figure S8 in Supporting Information S2). Under these conditions, the predicted mineral assemblage is dominated by tremolite, garnet, epidote, and paragonite.

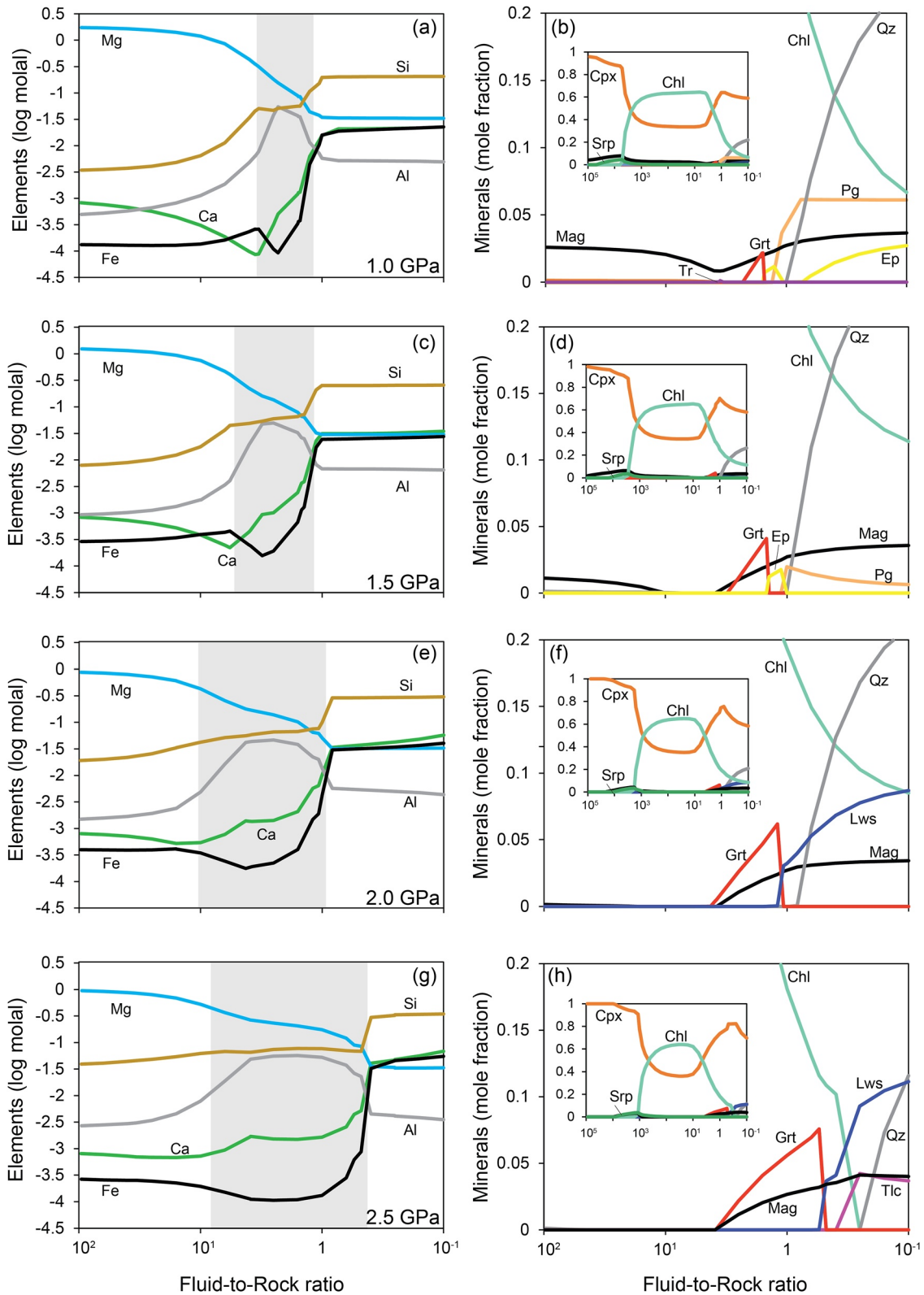


**Figure 11.** Predicted alteration mineralogy and fluid composition during high P-T metasomatism as a function of fluid-to-rock mass ratio. A fluid equilibrated with serpentinite (at  $f/r \sim 100$ ) is subsequently allowed to react with oxide gabbro at  $500^\circ\text{C}$ , 1.0–2.5 GPa (a–h). The  $f/r$  ratio decreases as gabbro is titrated into the fluid. Mineral abbreviations are from Whitney and Evans (2010). Zones highlighted in gray indicate elevated Al contents in the equilibrium pore fluids.



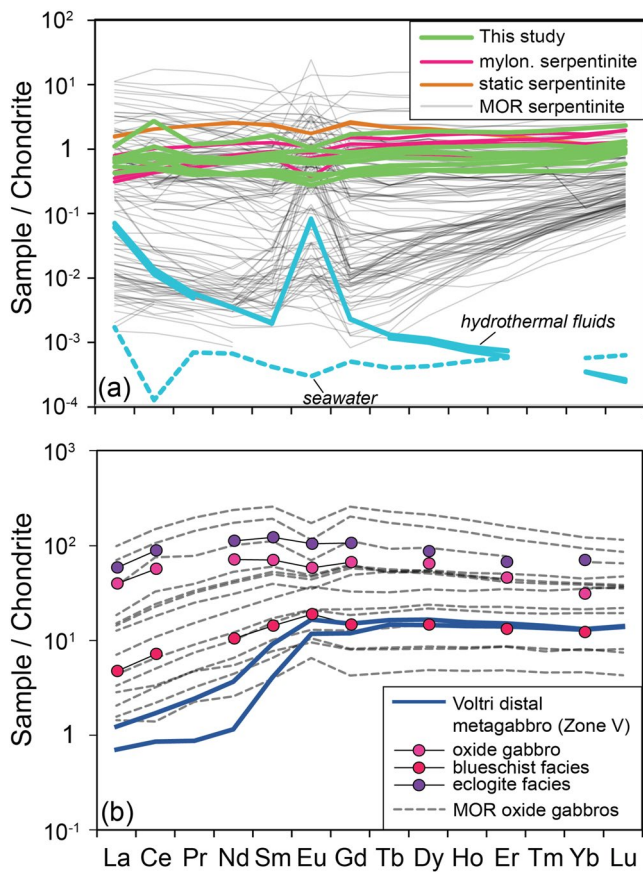


**Figure 12.** (a) Rare earth element systematics of Voltri serpentinites compared to the literature data of mylonitic and static serpentinites from Voltri Massif (Cannaò et al., 2016), compilation of serpentinites from mid-ocean ridges (Deschamps et al., 2013), hydrothermal fluids, and seawater (Douville et al., 2002). Concentrations of fluids are multiplied by 100 for scaling purposes. (b) Rare earth element systematics of the most distal LREE depleted eclogitic metagabbro of Zone V, compared to variably metamorphosed crustal rocks in the Voltri region (Tribuzio et al., 1996) and a literature compilation of oxide gabbros from the Atlantis Massif (Godard et al., 2009). This comparison shows that LREE depletion in subducted crustal rocks may occur at different stages over a wide range of  $P$ - $T$  conditions and in distinct tectonic settings, from oceanic environments to subduction zones. CI chondrite values are taken from McDonough and Sun (1995).

alteration of ultramafic rocks can impart significant changes in REE compositions (Klein et al., 2017; Paulick et al., 2006). Ocean-floor peridotites from passive margins and mid-ocean ridge settings are typically extensively to completely altered by seawater-derived hydrothermal fluids. While seawater shows fairly low REE abundances and a characteristic depletion in Ce relative to La (Elderfield & Greaves, 1982; Figure 12a), high-temperature hydrothermal fluids are enriched in Eu and can impart a positive Eu anomaly on serpentinitized peridotites (Douville et al., 2002; Paulick et al., 2006). The Voltri serpentinites lack strong positive Eu and negative Ce anomalies that would otherwise suggest reaction and equilibration with either black-smoker-type hydrothermal fluids or seawater, respectively (Cooperdock et al., 2018; Deschamps et al., 2013; Spandler et al., 2008), which also coincides with the low fluid-mobile element contents in the studied serpentinites. It is possible that such anomalies were obliterated or modified by subsequent metasomatism during subduction and exhumation; however, the absence of negative Ce anomalies and the presence of slightly negative Eu anomalies observed in most Voltri serpentinites calls for an open-system interaction of mantle rocks with relatively reducing aqueous fluids (German & Elderfield, 1990; Tostevin et al., 2016; Vitale Brovarone et al., 2020).

The same general sequence of minerals is predicted with decreasing  $f/r$  ratio at higher pressures (1.5–2.5 GPa) with some notable differences. With increasing pressure, tremolite becomes unstable whereas epidote, paragonite, lawsonite, and talc become stable. These reaction-path model predictions are consistent with our petrographic observation of epidote + paragonite found as inclusions within garnet. Importantly, while we did not find lawsonite, paragonite and epidote could be retrograde replacement products after lawsonite. Taken together, the reaction path models are consistent with metasomatism that could have occurred over a range of  $P$ - $T$  conditions from 450 to 550°C and from 1.0 to 2.5 GPa.

The model results for the reaction of serpentinite-equilibrated fluid with eclogite are presented in the supplement (Figure S9 in Supporting Information S2). Before reaction with eclogite, the composition of the fluid in equilibrium with serpentinite is predicted to be dominated by dissolved Mg in all models, with subordinate dissolved Si, Ca, Al, and Fe. With decreasing  $f/r$  ratios at 2.0 GPa and 450°C during reaction, the predicted sequence of minerals formed is antigorite + clinopyroxene → serpentine + clinopyroxene + chlorite → chlorite + clinopyroxene ± talc ± orthopyroxene ± quartz. At higher temperatures and similar pressure, garnet is predicted instead of talc. Magnetite is present in all model results. Note that the predicted minerals talc and orthopyroxene are not observed in Zones II to V.

## 4. Discussion

### 4.1. Constraints on the Origins of Serpentinite

Variably serpentinitized ultramafic rocks are widespread along slow- and ultraslow-spreading mid-ocean ridges, passive margins, and subduction zones (Deschamps et al., 2013; Kodolányi et al., 2012). To assess whether the Voltri serpentinites originally formed in an oceanic setting or in a subduction zone, we compare the measured trace element compositions and the <sup>87</sup>Sr/<sup>86</sup>Sr isotope ratios with those of serpentinites from different tectonic settings, along with representative compositions of seafloor hydrothermal fluids and seawater. The generally smooth and flat chondrite-normalized REE patterns of the Voltri serpentinites are similar to those of mantle rocks that experienced limited degrees of melting (Figure 12a). The elevated LREE/HREE ratios (e.g., La/Yb = 0.52–1.02) relative to the depleted MORB mantle (DMM = 0.53; Workman & Hart, 2005) are comparable to refertilized mantle impregnated by MORB melts in oceanic or in extensional settings (Deschamps et al., 2013; Kodolányi et al., 2012; Paulick et al., 2006; Rampone & Hofmann, 2012; Scambelluri et al., 2019). However, aqueous

The radiogenic  $^{87}\text{Sr}/^{86}\text{Sr}$  composition of the Voltri serpentinite (0.7083) cannot be explained by serpentinization of peridotite by less radiogenic Jurassic seawater ( $^{87}\text{Sr}/^{86}\text{Sr} = 0.707$ ) (Jones et al., 1994; Figure 6d). Rather, it requires subsequent modification by another fluid that carried more radiogenic, crustal-derived Sr before or during subduction. Cannà et al. (2016) examined the geochemistry of subducted, undeformed (static) and mylonitic serpentinites in the Voltri Massif. The more radiogenic Sr-isotope characteristics of mylonitic serpentinite were attributed to interaction with fluids derived from a sedimentary or crustal reservoir during the early stages of burial along the subduction interface. The chondrite-normalized REE compositions of our studied serpentinite resemble the mylonitic serpentinite but are distinct from the undeformed serpentinite domains in terms of LREE (Cannà et al., 2016). Even though un-subducted oceanic serpentinites in the neighboring Northern Apennine Ophiolite (Italy) were reported to show similarly radiogenic Sr-isotope ratios ( $^{87}\text{Sr}/^{86}\text{Sr} = 0.70337$  to 0.7086; Schwarzenbach et al., 2021), we favor the interpretation where the Sr isotope composition of our studied serpentinite was obtained during subduction in lieu of the textural and geochemical similarities with the mylonitic serpentinite studied by Cannà et al. (2016).

The magnetic susceptibilities of Voltri serpentinite is fairly low, and comparable to serpentinite formed at low temperatures ( $<200^\circ\text{C}$ ) at the Iberian Margin (Klein et al., 2014, 2017). However, the bulk-rock  $\text{Fe(III)}/\text{Fe}_T$  values of the Voltri serpentinite ( $\text{Fe(III)}/\text{Fe}_T \sim 0.3$ ; Figure 5d) are significantly lower than in completely serpentinized oceanic peridotites ( $\text{Fe(III)}/\text{Fe}_T > 0.84$ ; Klein et al., 2009, 2014). Similar trends in Alpine serpentinites have been attributed to the reduction of ferric to ferrous iron during prograde metamorphism of lizardite and chrysotile to antigorite and the destabilization of magnetite (Debret et al., 2014, 2016). In Alpine serpentinites, it has been suggested that ferric iron can be reduced to ferrous iron while magnetite is destabilized during prograde metamorphism (Debret et al., 2014, 2016); however, recent studies call this inference into question as Alpine serpentinites have experienced distinctly different metamorphic conditions and their protolith compositions remain incompletely understood (Evans & Frost, 2021). It remains unclear whether the serpentinite studied here originally contained magnetite that destabilized during metamorphism or if oceanic serpentinization did not produce significant magnetite to begin with. If the REE patterns were not significantly modified during subduction, the lack of an Eu anomaly associated with high-temperature ridge crest hydrothermal fluids (Douville et al., 2002) is consistent with serpentinization at moderate temperatures, which would point to limited magnetite formation during serpentinization. The lower  $\text{MgO}/\text{SiO}_2$  of serpentinites relative to the terrestrial melting array of peridotites would be consistent with MgO loss from brucite breakdown during subduction or possibly during weathering prior to subduction (Klein et al., 2020; Peters et al., 2020). The low  $\text{Fe(III)}/\text{Fe}_T$  values would be consistent with reduction of Fe(III) to Fe(II) during metamorphism (Debret et al., 2014, 2016). If no magnetite was initially formed during serpentinization (and considering that the studied Voltri serpentinites do not contain brucite), this could have been accommodated by reduction of Fe(III) to Fe(II) in serpentine. Overall, the results presented in this study are consistent with partial serpentinization in an oceanic setting with subsequent modifications of its chemical and mineralogical characteristics during high-pressure metamorphism and deformation.

#### 4.2. Constraints on the Formation of Distal Eclogitic Metagabbro

The REE patterns of the most distal LREE-depleted metagabbros provide clues on the origin of their mafic protolith. The metagabbro from Zone V displays the most depleted LREE concentrations among the mafic rocks studied here. Previous studies have suggested that oceanic (Fe, Ti-rich) oxide gabbros were likely the protolith of the metagabbro in the study area (Malatesta et al., 2012a; Tribuzio et al., 1996). The abundance of the Ti-rich phases rutile and ilmenite, as well as the elevated bulk-rock  $\text{FeO}^*$  (= total Fe as FeO) and  $\text{TiO}_2$  contents closely resemble those of oxide gabbro from the International Ocean Drilling Program (IODP) Site U1309 (Atlantis Massif), but are distinctly different from other gabbroic lithologies from the same IODP site (Godard et al., 2009; Figure 13a). The chondrite-normalized trace element concentrations of the LREE-depleted metagabbro are plotted along with oceanic oxide gabbros from IODP Site U1309 (Figure 12b). Oceanic oxide gabbros show a wide range in chondrite-normalized compositions and Eu anomalies. Samples with elevated REE abundances show more pronounced negative Eu anomalies. Conversely, samples that are depleted in REE, especially in LREE, show weak positive Eu anomalies, which resemble the LREE-depleted (Zone V) metagabbro in this study. Alternatively, LREE depletion has been suggested to also occur at the gabbro-to-eclogite transition during prograde subduction (Becker et al., 2000; John et al., 2004; Tribuzio et al., 1996). For example, Tribuzio et al. (1996) investigated LREE-depleted oxide gabbro-derived lithologies equilibrated at blueschist and eclogite-facies conditions in Voltri and attributed the LREE depletion to the absence or destruction of LREE-compatible epidote minerals

during prograde metamorphism. These observations imply that LREE depletion can occur at different stages over a wide range of  $P$ - $T$  conditions and in distinct tectonic settings, from oceanic environments to subduction zones. Without additional constraints it remains challenging to differentiate a possible inherited LREE-depletion prior to subduction from LREE-depletion during high-pressure metamorphism. However, considering the very short length-scales, we infer that the lower chondrite-normalized LREE concentrations of Zone V relative to adjacent zones suggest that LREE depletion may have occurred during prograde subduction and contributed to the LREE budget of the adjacent metasomatic reaction zones.

### 4.3. Controls on the Compositions of the Studied Metasomatic Reaction Zones

The overall distribution of major and trace elements in zones (II-IV) between serpentinite and eclogitic metagabbro may result from the interplay of three processes: (a) mass transfer by mechanical mixing of rocks, (b) mass transfer by diffusion across a chemical gradient, and/or by advection of external fluids. We discuss the potential contributions of each process below.

#### 4.3.1. Mechanical Mixing

Mechanical mixing of two or more chemically distinct rocks will result in a new rock with a composition that lies on a mixing line in between the endmembers (Bebout & Barton, 2002; Gorman et al., 2019). However, the bulk compositions of the metasomatic rocks in Zones II-IV do not lie along the bulk mixing trend between the most distal samples of Zone I and V (Figure 13b). Accordingly, the amphibole- and chlorite-rich assemblage (Zone II) along the field contact was not a simple binary mixture of components from serpentinite and distal metagabbro. This is supported by the lack of correlation between Ni and Cr, which would otherwise be expected if the metasomatic rocks were formed by mechanical mixing of two endmember compositions (Gorman et al., 2019; Penniston-Dorland et al., 2014). Rather, Ni and Cr show large variations with trends similar to that of bulk-rock MgO concentration, which resemble sigmoidal profiles that are suggestive of diffusive transport from serpentinite to metagabbro (Figure 6b). In addition, we used the ratios of two fluid-immobile elements (Figure 13b) and the bulk-rock  $^{87}\text{Sr}/^{86}\text{Sr}$  isotope ratio as they are highly sensitive to protolith chemistry but are largely insensitive to fluid metasomatism. The clear step-wise pattern in  $^{87}\text{Sr}/^{86}\text{Sr}$  isotope ratios separating Zones II to V from Zone I at the lithologic boundary does not support a mechanical mixing process as a key contributor to the compositional variability observed in the transect (Figure 6d). Likewise, the Sc concentration shows a step-function similar to the trace element ratios and Sr isotopes, reflecting its limited fluid mobility (Figure 6b). Hence, in contrast to the Catalina Schist (USA), where mechanical mixing of ultramafic and mafic blocks has been documented (Gorman et al., 2019; Penniston-Dorland et al., 2014), we found no evidence for mechanical mixing along the serpentinite-metagabbro contact studied here. It is also possible that shearing and deformation may have transposed and even stripped off metasomatic reaction zones along lithologic margins (Ague, 2007). However, this possibility can be ruled out in our studied transect based on the lack of geochemical evidence for mechanical mixing, as well as the contact-perpendicular sampling strategy in both the serpentinite and metagabbro, which would have captured any transposed reaction zones along the contact.

#### 4.3.2. Mass Transfer via Advective and/or Diffusive Transport

The juxtaposition of different and chemically disparate rock-types favors fluid-mediated diffusive mass transfer (Bickle & McKenzie, 1987; Ferry & Dipple, 1991; Korzhinskii, 1965; Thompson, 1975). In a setting that is similar to the one examined here, Pogge von Strandmann et al. (2015) investigated metasomatism in an asymmetrical reaction zone between serpentinite and metatuffite in Syros (Greece) and observed strong Mg-isotope fractionations in the metatuffite proximal to the contact in a chlorite-rich zone. They showed that fluid-mediated diffusive transport across the transect involved multiple components, where the diffusive fluxes of components were driven by distinct chemical potentials. The extent of mass transfer was primarily controlled by the activities, solubility, and relative mobilities of the components across the contact. At Voltri, chemical and mineralogical changes along the transect can provide additional constraints on the mode of mass transfer between serpentinite and metagabbro. For instance, the sigmoidal patterns in bulk-rock MgO,  $\text{H}_2\text{O}$ , and Ni already suggest diffusive transport across the serpentinite-metagabbro transect.

In a purely diffusive regime without advective fluid flow, we would expect mineralogical reaction zones on both sides of the serpentinite-metagabbro contact via bi-directional metasomatism (Bach et al., 2013; Bach & Klein, 2009; Korzhinskii, 1965, 1968; Miller et al., 2009; Pogge von Strandmann et al., 2015; Thompson, 1975),



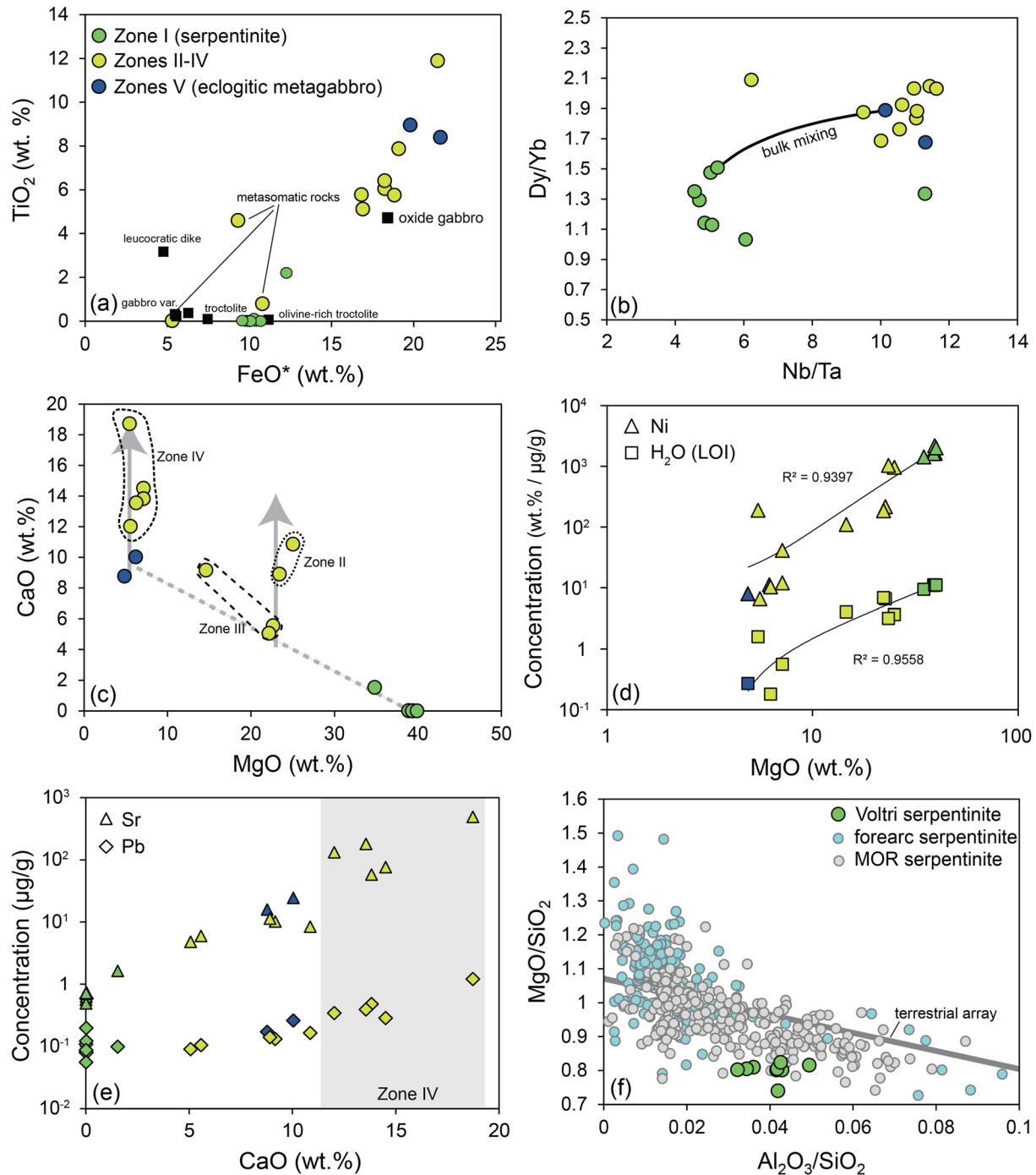


**Figure 13.** Variations among major and trace elements, and water. (a) TiO<sub>2</sub> versus FeO\*, (b) Dy/Yb versus Nb/Ta, (c) CaO versus MgO, (d) Ni and H<sub>2</sub>O (represented by LOI) versus MgO, (e) Pb and Sr versus CaO, and (f) MgO/SiO<sub>2</sub>/Al<sub>2</sub>O<sub>3</sub>/SiO<sub>2</sub> of studied serpentinite along with literature data (Peters et al., 2017b) of mid-ocean ridge and forearc serpentinites. Data from Godard et al. (2009) in (a) are shown as black squares. The bulk mixing line between serpentinite and metagabbro in (b) was calculated using the composition of distal eclogitic metagabbro and serpentinite assuming that their compositions were least affected by the mass transfer between the two lithologies. In (c), the dashed line connecting Zone I and V shows that Zones II, III, and IV require addition of CaO as depicted in gray arrows. In (d), the lines display the correlations among samples in terms of Ni versus MgO ( $R^2 = 0.9397$ ) and H<sub>2</sub>O versus MgO ( $R^2 = 0.9558$ ). The gray zone in (e) marks samples from Zone IV.

which would result in Si-metasomatism of serpentinite and Mg-metasomatism of metagabbro. Yet, talc-alteration of serpentinite by Si-rich fluids is limited and there is no systematic increase in the modal proportion of talc in serpentinite toward the contact that would be expected in the absence of unidirectional advective fluid flow. The limited amount of talc in the studied serpentinite is similar to that of unsubducted serpentinite in the neighboring

Northern Apennine Ophiolite (Italy), which suggest that the amount of talc in Voltri serpentinite was likely set in an oceanic setting, that is, prior to subduction (Schwarzenbach et al., 2021). Accordingly, the asymmetry of the reaction zones could have resulted from unidirectional advective fluid flow that transported Mg from the serpentinite into the gabbro. To explain the asymmetry of the Syros transect, Pogge von Strandmann et al. (2015) suggested that the lack of talc-alteration on the serpentinite side can be attributed to congruent dissolution of serpentinite and Si export by contact-parallel fluid flow. However, advective mass transport was ruled out because the velocity of advection would have outpaced the mass transfer via diffusion (or the rate at which equilibrium partitioning can be attained) and would have destroyed the prominent negative  $\delta^{26}\text{Mg}$  isotope fractionation that can only be achieved via diffusion.

Alternatively, the lack of talc alteration in serpentinite from Voltri and Syros may reflect the lack of chemical affinity for such a reaction to proceed at subduction zone  $P$ - $T$  conditions. Even though talc would be thermodynamically stable at such  $P$ - $T$  conditions, the formation of talc at the expense of serpentine (i.e., antigorite + 30  $\text{SiO}_{2(aq)} = 16\text{talc} + 15\text{H}_2\text{O}_{(l)}$ ) may not be favored. To test this, we evaluated the  $a\text{SiO}_{2(aq)}$  in a fluid buffered by metagabbro and also modeled the reaction of such a fluid with serpentinite over a range of  $P$ - $T$  conditions. Our thermodynamic calculations predict that the  $a\text{SiO}_{2(aq)}$  of the fluid buffered by gabbro exceeds the  $a\text{SiO}_{2(aq)}$  of the serpentine-talc equilibrium, despite the pressure-dependent increase in  $a\text{SiO}_{2(aq)}$  buffered by the serpentine-talc equilibrium (Figures 14e and 14f). Accordingly, simple univariant phase equilibria would suggest that conditions were favorable to form talc at the expense of serpentine. However, the chemical affinity depends on the Gibbs free energy of the reaction at the temperature and pressure, which is affected by the equilibrium speciation of dissolved species. The reaction-path models at 400–500°C predicted a talc-free alteration assemblage that is dominated by garnet + chlorite + serpentine (Figures 14a–14d). The elevated activities of Al and Ca in the fluid may have inhibited the saturation of talc by promoting the formation of garnet and chlorite. In particular, the solubility of Al in aqueous fluids has been shown to increase significantly at high  $P$ - $T$  conditions due to the formation of aluminosilicate complexes (Manning, 2007). This favors the saturation of Al-bearing phases, which likely explains the occurrence and abundance of chlorite-rich assemblages in reaction zones found in Voltri and possibly in other settings, where similar exhumed high-pressure rocks are found. Our findings are consistent with previous studies on talc schist in Santa Catalina Island (USA) which suggest that the Si/Al ratio of rocks and fluids plays a key role in stabilizing chlorite over talc (Bebout & Barton, 2002). However, the formation of talc in subduction zones can be facilitated where excess Si is available, such as in mélanges of Si-rich sediments and serpentinite, possibly at higher temperatures (Breeding et al., 2004; Miller et al., 2009). Another process that can yield sizable talc deposits in both subduction zones and orogenic belts is mineral carbonation of serpentinite, facilitated by decarbonation of metamorphosed carbonate-rich sediments (Spandler et al., 2008).

Importantly, our thermodynamic calculations suggest that an external fluid is not required to explain the absence of talc and the observed asymmetry of reaction zones between serpentinite and metagabbro simply because the formation of talc is not favored. This would also imply that the asymmetrical reaction zones may not be taken as evidence against bidirectional diffusive transfer as changes may manifest differently on either side of a lithologic contact depending on thermodynamic controls. These findings are further supported by the sigmoidal concentration profiles of Mg, Ni, and  $\text{H}_2\text{O}$  that point to diffusive transfer from serpentinite to metagabbro (Figures 3a and 5b). The diffusive influx of Mg, Ni, and  $\text{H}_2\text{O}$  from serpentinite into the metagabbro led to the formation of hydrous minerals in Zones II and III and roughly similar bulk-rock MgO concentrations in these two zones. If the mass transfer between serpentinite and metagabbro is driven by the differences in the activity of Mg species, the minerals that are forming under this activity gradient are expected to record systematic variations in their mineral compositions (Korzhinskii, 1968; Miller et al., 2009; Pogge von Strandmann et al., 2015; Thompson, 1970). Evidence for that is provided by the increasing Mg contents of chlorite and amphibole toward the contact (Figures 3b and 3c).

Mass-balance constraints suggest that the formation of chlorite-rich schist at the expense of metagabbro in Zone III, not only requires the addition of Mg ( $\sim 84\text{ kg/m}^2$ ) and  $\text{H}_2\text{O}$  ( $\sim 40\text{ kg/m}^2$ ) but the removal of Ca ( $\sim 10\text{ kg/m}^2$ ) as well (Figure 13c; Figure S10 in Supporting Information S2). Note that the low concentrations of CaO in Zone III (Figure 5b) cannot be explained with simple dilution due to the addition of Mg. Indeed, mass balance calculations suggest that Ca was likely redistributed into the adjacent Zones II and IV, which led to the stabilization of Ca-amphibole and epidote. Zone IV experienced a significant enrichment in Ca ( $\sim 104\text{ kg/m}^2$ ) whereas Zone II displays a more muted Ca enrichment. Zone II and III likely experienced significant Ca losses during the

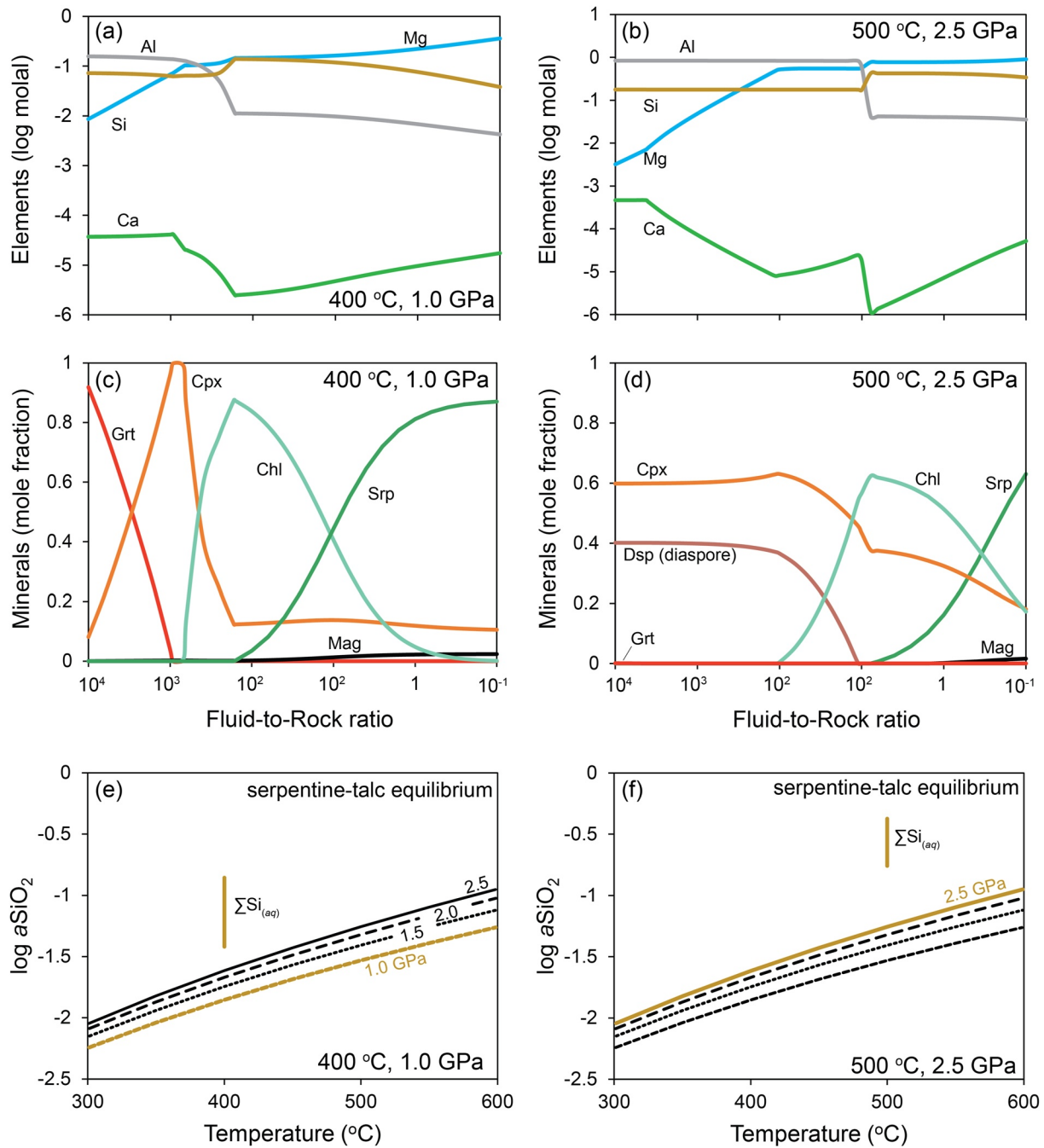


**Figure 14.** Predicted alteration mineralogy and fluid composition during high P-T metasomatism as a function of fluid-to-rock mass ratio. A fluid equilibrated with gabbro (Di + An, at  $f/r > 1000$ ) is subsequently allowed to react with serpentinite at 400–500°C, 1.0–2.5 GPa (a–d). The  $f/r$  decreases as serpentinite is titrated into the fluid. Mineral abbreviations are from Whitney and Evans (2010). Lower panels: Activity of silica buffered by serpentine-talc equilibrium from 1.0 to 2.5 GPa. The composition of dissolved Si from the reaction-path models plotted above the univariant line in the stability field of talc (e–f).

formation of chlorite schist but later Ca redistribution into Zone II balanced out the initial Ca loss. We note that the bulk-rock CaO concentration correlates positively with the bulk-rock REE and fluid-mobile element patterns. Therefore, the bulk-rock distribution of these trace-elements may be intimately linked to the distribution of Ca. In particular, the dominant transport of Ca into the more interior parts of the metagabbro explains the bulk-rock REE and fluid-mobile element concentration profiles (Figures 4b and 12c).



The maximum enrichment of LREE and fluid-mobile elements occurs within Zone IV, which also shows the highest CaO concentration, whereas the maximum enrichment of HREE is in Zone III (Figures 5a and 5c). The concentration profiles of Eu and Gd (MREE), which are geochemically intermediate between LREE and HREE, show peak enrichments coinciding with LREE and HREE enrichments. This trend is interpreted to indicate diffusion of trace elements within the metagabbro from Zones II-III into the more interior Zone IV. We infer that the observed lag in the position of peak enrichments between LREE and HREE reflects the difference in their bulk diffusivities, with LREE diffusing faster than HREE (with MREE having an intermediate bulk diffusivity). Assessment on bulk diffusion in natural polymineralic rocks requires constraints on the diffusivities of each constituent mineral, grain sizes, variations in interconnectivity of fast pathways (e.g., pore fluids), and differences in the concentration of the diffusing element (diffusant) within each mineral phase or fluid (Watson & Baxter, 2007). All of these factors are difficult to constrain. Considering that the dominant mass transfer mechanism in our studied transect is diffusion mediated by interconnected pore fluids, transport through interconnected porosity becomes efficient if a significant amount of the REE is dissolved in the pore fluid. This in turn is a function of REE solubility in aqueous fluids. Fluid-rock partitioning studies display higher concentrations in LREE than HREE in aqueous fluids over a range of high *P-T* conditions (Kessel et al., 2005). The generally higher solubility of LREE relative to HREE would amount to their higher bulk diffusivity, if other factors mentioned above are set constant. Our interpretation of higher LREE diffusivities in pore fluids is further supported by the coinciding positions of LREE and fluid-mobile element peak enrichment. We infer that these trace elements are mainly hosted by epidote in Zone IV that is formed due to Ca addition (Figure 13e). While we did not measure the trace element composition of epidote in situ, previous studies have shown that LREE are compatible in epidote-bearing rocks from subduction zones (Ague, 2017; Carter et al., 2015). The strong correlations between bulk-rock CaO and LREE as well as the similarity in the position of peak enrichment (Figure 5a, yellow bar) suggest that their mobilization and redistribution occurred simultaneously. In particular, the transport of Ca into Zone IV led to the formation of epidote minerals which have high affinity for LREE. The decreasing concentrations in CaO and LREE from Zones IV to V are also consistent with diffusion of these elements from Zone III into the metagabbro. The co-diffusion of Ca and LREE leads to the formation of Ca-rich minerals (e.g., epidote) nearby that then become important hosts for these trace elements, preventing their further mobilization. The lack of a mineral host for the REE in Zones II and III is consistent with the lack of an REE enrichment in these zones. The diffusion of components toward the metagabbro may have contributed to the asymmetrical geometry of the reaction zone between the serpentinite and metagabbro, with enhanced alteration on the metagabbro side. On the other hand, trace element changes in the serpentinite are less pronounced. This is exemplified by the enrichment in  $(La/Sm)_N$  in the serpentinite that is most proximal to the contact (Figure S7 in Supporting Information S2).

#### 4.4. Metamorphic and Mass Transfer History

In this section we further constrain the relative timing of metasomatism by integrating the *P-T* estimates derived from pseudosection and garnet isopleth models with Sr-isotope systematics and reaction path modeling. Consistent with Cannadò et al. (2016), serpentinitization of peridotite in the Voltri Massif occurred at least partly in an oceanic setting whereas the Sr-isotope composition of serpentinite was likely set during the early stages of subduction. Field evidence suggests that the serpentinite and oxide gabbro were likely in contact while in an oceanic setting prior to subduction (Manatschal & Müntener, 2009; Piccardo, 2013; Scambelluri et al., 1995a). This is supported by field exposures of juxtaposed serpentinite and gabbroic bodies similar to our studied transect that are found in neighboring localities, such as the Northern Apennines that had never been subducted (Lagabrielle & Lemoine, 1997). However, our petrographic and geochemical evidence suggest that the mass transfer process that formed the metasomatic reaction zones likely occurred in a subduction zone setting.

Pseudosection and garnet isopleth modeling allows us to determine whether mass transfer between serpentinite and metagabbro occurred during prograde, peak, or retrograde metamorphism. Results from pseudosection models yielded *P-T* estimates for the onset of eclogitization (~430–470°C, 2.2–2.5 GPa) up to peak eclogite-facies metamorphism (~520°C, ~2.5 GPa) for Zones IV and V (Figure 9f). While the bulk composition during the earliest stages of garnet growth in sample B03 was possibly different from measured, our calculations likely represent a close approximation. However, it remains unclear whether the mineralogical and chemical differences between Zones IV and V developed during prograde-to-peak evolution or slightly post-peak (i.e., during near-isothermal decompression). The most prominent chemical and mineralogical changes can be attributed to the addition of Mg to the metagabbro that caused the formation of chlorite and the redistribution of Ca.

Here we determine the timing of chlorite formation in Zones II and III and the enrichment of Ca in metagabbro of Zone IV relative to that in Zone V. We rely on garnet core-to-rim element variations in these zones to resolve the relative timing of Ca enrichment (Figures 3a and 4). Garnet cores in Zone IV and V have similar Ca contents, which suggests that bulk-rock Ca composition are similar at the initiation of garnet growth along the prograde path. The Ca contents of garnet in Zone IV (B06 and B07) increases systematically from core to rim, which is the opposite trend for garnet in Zone V. In addition, anhedral garnet in Zone III has higher Ca contents than garnet in Zones V but overlaps with garnet from Zone IV. These results imply that Ca becomes more available during the growth of garnet in Zones III and IV. Since garnet from the more distal sample B07 in Zone IV displays less pronounced core-to-rim Ca enrichment than in sample B06, this suggests that Ca availability diminishes toward the metagabbro interior. We suggest that the bulk Ca-enrichment in Zone IV occurred or at least started during prograde eclogite-facies conditions. While garnet from exhumed (ultra) high-P metamorphic rocks in subduction zones have substantial Ca contents (8–9 wt. % CaO) for example, in Sifnos, Greece and Lago di Cignana, Italy (Dragovic et al., 2012; Groppo et al., 2009), these CaO concentrations are below those measured in garnet rims in Zone IV (up to ~12 wt. % CaO). If the Ca-enrichment in Zone IV would have occurred prior to subduction or even prior to the onset of garnet growth, subsequent eclogite-facies metamorphism would have formed garnets that would be significantly more grossular-rich (i.e., almandine-poorer) than the garnet analyzed in our samples (Figure 9c). Therefore, pre-subduction and pre-peak Ca-enrichment in Zone IV seem unlikely, which provides additional support for Ca enrichment occurring during prograde subduction up to peak depths.

The simultaneous addition of Mg and H<sub>2</sub>O, and removal of Ca from the precursor metagabbro are necessary to form chlorite-rich schists in Zone III (Figures 12c and 12d). We have shown that Ca along with trace elements released from this process are redistributed into adjacent Zones II and IV. Therefore, the chlorite-rich schists in Zone III must have formed before or at the same time as Zones II and IV during prograde subduction. Fluid-rock interactions likely continued during peak and post-peak eclogite-facies metamorphism based on petrographic evidence of garnet replacement by chlorite (Figure 15). Evidence for subsequent retrograde overprinting and local re-equilibration during a near-isothermal decompression to ~1.0 GPa includes the presence of albite in Zone IV and V, titanite rims around rutile and ilmenite in Zones II-V, as well as calcic rims on sodic-calcic amphiboles (Malatesta et al., 2012b; Starr et al., 2020; this study).

Additional support is provided by the reaction-path models. One of our simplest reaction-path models, which explores the possibility that a single fluid-mediated mass transfer event occurred during prograde to peak eclogite-facies metamorphism predicts a succession of mineral assemblages that closely matches the ones observed in the transect. This implies that a single fluid-mediated mass transfer event may have occurred and set the bulk compositions of the metasomatic zones during prograde to peak eclogite-facies metamorphism. However, the duration of this event remains undetermined. We have shown that only reaction-path models that used a gabbroic mineral assemblage successfully predict a succession of mineral assemblages that closely matches the one observed in our studied transect whereas those with eclogitic mineral assemblage do not. This is consistent with pseudosection models that suggest the completion of that mass transfer prior to retrogression. The difference in the pressures estimated by pseudosection and garnet isopleth models (~2.2 GPa for garnet nucleation) and reaction-path models that successfully reproduced the mineral sequence may reflect either a reaction overstepping where garnet nucleation occurred at *P-T* conditions greater than initial garnet stability or inaccuracies in the effective bulk composition used for the pseudosection modeling. We speculate that garnet nucleation may have been limited by the availability of fluid that promotes faster nucleation and growth. Additionally, we suspect that the effective bulk composition is changing as garnet grows. This could explain the discrepancy in the estimated garnet modal abundances (i.e., 2 and 5 vol. % for samples B10 and B06, respectively) at *P-T* conditions constrained by garnet crystal core chemistry.

Finally, while our reaction path models successfully reproduce the observed mineral sequence at pressures as low as 1 GPa, this is a minimum estimate, and indeed, mass transfer may have initiated at greater depths. Nonetheless, both models suggest that mass transferred occurred or at least initiated during prograde subduction. This is followed by a near-isothermal decompression with limited mass transfer, where metasomatic zones primarily underwent local re-equilibration and recrystallization (Figure 15).

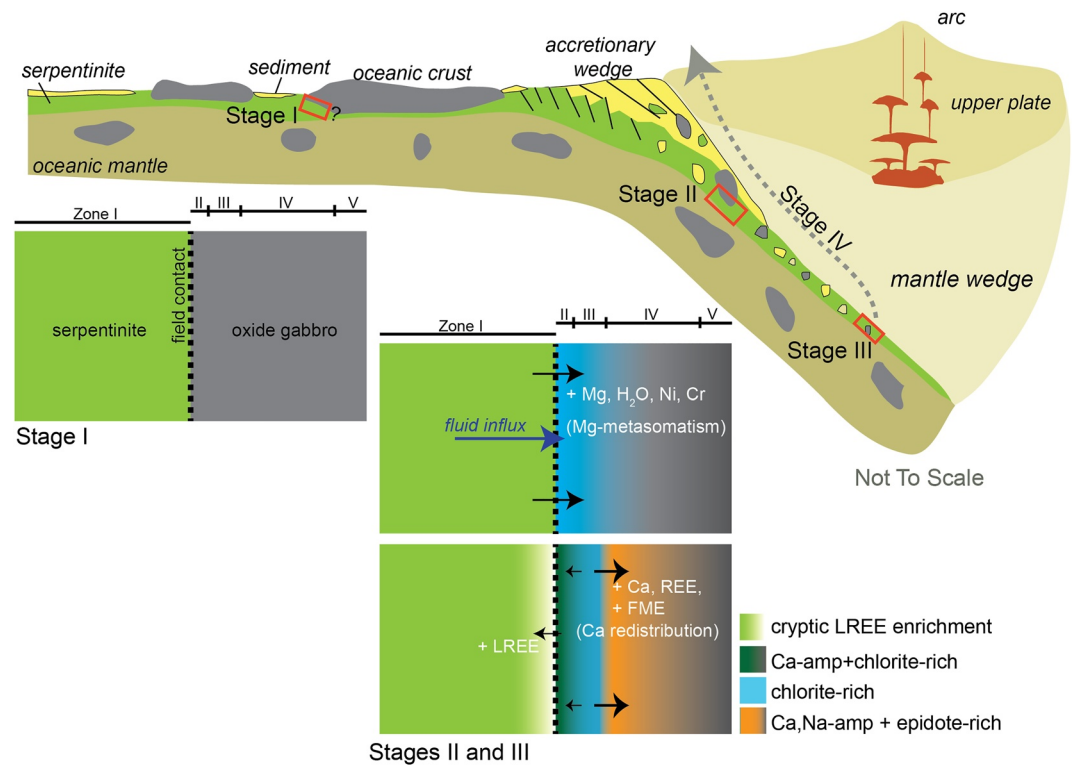


**Figure 15.** Summary of possible tectonic settings of mass transfer recorded by the studied serpentinite-metagabbro transect. Juxtaposition between serpentinite and metagabbro may have occurred in an oceanic setting prior to subduction in Stage I. Fluid-mediated mass transfer led to the development of metasomatic reaction zones that record significant Mg metasomatism and Ca redistribution in subducted metagabbro during prograde to peak eclogite-facies metamorphism in Stages II and III. Subsequent exhumation accompanied by limited mass transfer and local re-equilibration are displayed in Stage IV.

#### 4.5. Mg-Metasomatism Is Favored in Subduction Zones

The strong positive correlations between bulk-rock concentrations of MgO and Ni, and bulk-rock MgO and LOI in all the samples, as well as the continuously decreasing concentration profiles of these elements (Figure 12d), suggest that the fluids equilibrated with serpentinite prior to metasomatism of metagabbro (Miller et al., 2009; Pogge von Strandmann et al., 2015). Phase equilibrium and thermodynamic studies have suggested that subducting oceanic crust can produce a continuous flux, and sometimes, episodic pulses of aqueous fluids through a series of mineral dehydration reactions up to eclogite-facies metamorphic conditions (Hacker, 2008; Schmidt & Poli, 1998, 2014; van Keken et al., 2011). This assures the availability of aqueous fluids at least along the slab-mantle interface. Of particular importance is the breakdown reaction of antigorite and brucite to form olivine and water, as this reaction is well-documented in the Vara serpentinite locality, which is in close proximity to our studied serpentinite (Cannaò et al., 2016; Scambelluri & Rampone, 1999), as well as in the neighboring Erro-Tobbio locality (Scambelluri et al., 1991, 1995b).

Recognizing possible regional sources of fluids in our study area, our thermodynamic calculations suggest that  $\text{Mg}(\text{OH})_{2(aq)}$  could have been a dominant species in the fluid that equilibrated at high concentrations with serpentinite at high  $P$ - $T$  in a subduction zone. This suggests that the propensity for Mg-metasomatism by fluids that equilibrated with serpentinite is enhanced in subduction zone settings when compared with oceanic settings where the concentrations of dissolved Mg in hydrothermal fluids are low (cf. Bach et al., 2013). However, the differences in the predicted speciation and activities between low and high (1.0–2.5 GPa) pressure conditions may also in part reflect the limited availability of thermodynamic data for dissolved species at such high-pressure. The few available experimental studies and reports of fluid inclusions from high-pressure rocks in the Western Alps strongly suggest elevated dissolved Mg and elevated salinity in aqueous fluids (Iacovino et al., 2020; Scambelluri et al., 1997), lending credence to the thermodynamic predictions presented here. If these predictions are correct, the abundance of serpentinite in subducted oceanic lithosphere, the overlying mantle wedge, and the slab-mantle



interface would represent possible sites of where fluids can obtain high concentrations of dissolved Mg regardless of sources and compositions of the infiltrating fluid. In this scenario, the composition of a fluid that originates elsewhere (e.g., breakdown of hydrous minerals from subducted, hydrothermally-altered igneous rocks and sediments) is modified as it infiltrates the serpentinite already present along the subduction interface. The resulting composition of the pore fluid buffered by serpentinite likely resembles the characteristic fluid composition (i.e., Mg-rich and Al, Fe, Ca-poor) even though the starting fluid had a different composition before it infiltrated and equilibrated with serpentinite. As these fluids infiltrate through and re-equilibrate with serpentinites, the intrinsic porosity of serpentinites (Tutolo et al., 2016) can store large amounts of pore fluids that may promote fluid-mediated diffusion and Mg-boundary metasomatism in juxtaposed crustal rocks.

#### 4.6. The Need for Solid Solutions in Reaction Path Models to Infer Redox Conditions in Subduction Zones

The present study may also provide clues about prevailing redox conditions during Mg-metasomatism of gabbros. The Fe(III)/Fe<sub>T</sub> of altered metagabbro in Zones II to IV is generally elevated when compared with metagabbro in Zone V. This could either reflect the pre-existing heterogeneity of the oxide gabbro precursor, or a result of oxidation during metasomatism (Figure S8 in Supporting Information S2). We attempted to use the reaction path models to constrain  $fO_2$  as the fluid that previously equilibrated with serpentinite reacts with gabbro. Even though the models successfully reproduced the observed succession of mineral assemblages, they failed to reproduce the complexity of the natural system. One shortcoming of the models is attributed to the lack of solid solutions of Mg-Fe minerals in the thermodynamic database, most notably greenalite or cronstedtite in serpentine, the Fe(OH)<sub>2</sub> component of brucite, and the andradite component of garnet. Because the Fe(III)/Fe<sub>T</sub> of the modeled serpentinite was dictated by magnetite as the only Fe-bearing phase, the modeled  $fO_2$  of the fluid in equilibrium with the serpentinite likely differed from that of the natural system. The lack of Fe(III)-components in the minerals predicted to form during metasomatism of gabbro introduce errors in the calculation of  $fO_2$ .

#### 4.7. Geochemical and Petrophysical Implications of Fluid-Rock Interactions in Subduction Zones

Fluid-mediated mass transfer between juxtaposed chemically disparate rock types can lead to the formation of a variety of metasomatic rocks with geochemical and petrophysical properties that are distinct from their precursors (Ague & Nicolescu, 2014; Angiboust et al., 2011, 2014; Bloch & Hofmann, 1978; Breeding et al., 2004; King et al., 2006; Miller et al., 2009; Mori et al., 2014; Penniston-Dorland et al., 2014; Pogge von Strandmann et al., 2015; Sanford, 1982). We have shown that serpentinite in subduction zones could produce fluids that are poor in Al, Fe, and Ca (<0.001 molal at 1.0–2.5 GPa) but may contain substantial amounts of dissolved Mg (e.g., 1.0–2.4 molal at 1.0 GPa; 0.6–1.1 molal at 2.5 GPa) through fluid-rock equilibration. This process is different from in-situ and active serpentinitization of the shallow forearc mantle, which produces Mg-poor, Ca-rich fluids (e.g., Mottl et al., 2004). These serpentinite-buffered fluids lead to Mg-metasomatism of mafic rocks and favor the ubiquitous formation of chlorite. Mg-chlorite is a rheologically weak metasomatic mineral that can contain up to ~13 wt. % water and be stable up to 800°C at subarc depths (Okamoto et al., 2019; Pawley, 2003).

Thermodynamic predictions suggest that the distinct chemical potentials of dissolved species in equilibrium with serpentinite and gabbroic mineral assemblages can drive diffusive mass transfer. The asymmetrical geometry of the metasomatic reaction zone in gabbro and the lack of talc alteration of serpentinite in the studied transect underlines the lack of sufficient thermodynamic drive to form talc at the expense of serpentine at high  $P$ - $T$  conditions in subduction zones (Figure 14). This is in contrast to the ubiquitous occurrence of talc-altered serpentinites that are juxtaposed to gabbro in oceanic settings (Bach et al., 2004, 2013; Paulick et al., 2006). A lack of extensively talc-altered serpentinite in subduction zones (Deschamps et al., 2013; Peters et al., 2017a) would likely affect the strength of the plate interface and the physical mechanisms controlling the coupling-decoupling depth in subduction zones. Owing to its high-pressure stability and rheological properties, the breakdown of talc has been suggested to reflect the downdip transition from a decoupled shear zone to a fully coupled plate interface (Peacock & Wang, 2021). Our thermodynamic calculations suggest that the formation of talc at the expense of serpentine by Si-metasomatism (via the reaction: antigorite + 30SiO<sub>2(aq)</sub> = 16talc + 15H<sub>2</sub>O<sub>(l)</sub>) may be more limited during subduction when compared with low pressure Si-metasomatism such as in oceanic settings where lower SiO<sub>2(aq)</sub> activities suffice to drive talc alteration. In subduction zones, talc-alteration of serpentinite is likely limited to settings where serpentinite and silica- or carbonate-rich sediments are juxtaposed, whereas

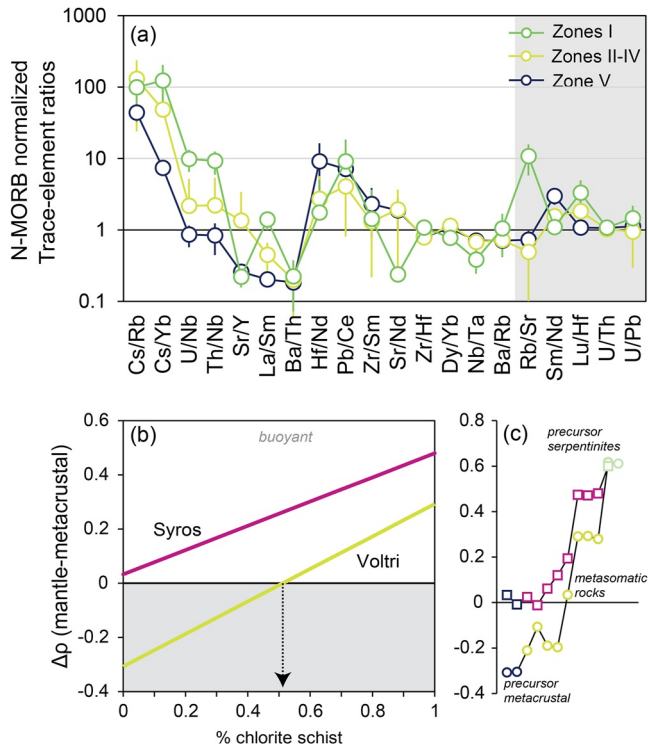


**Figure 16.** (a) N-MORB normalized trace element ratios of the entire serpentinite-metagabbro transect. Gray shaded ratios are radiogenic parent-daughter isotope pairs (b) Bulk density changes of precursor mafic crustal rock relative to mantle peridotite (DMM) as a function of chlorite content. (c) Bulk densities of serpentinite, metacrystal, and metasomatic rocks relative to mantle peridotite in Voltri Massif (this study) and Syros (Miller et al., 2009). N-MORB values are from Gale et al. (2013).

juxtaposition of gabbro (mafic crustal) and serpentinite would favor chlorite over talc. If the coupling-decoupling transition between the subducting plate and overriding mantle is related to the presence of talc, the juxtaposition of ultramafic rocks with sediment may be crucial (Abers et al., 2020; Marshall & Schumacher, 2012; Wada & Wang, 2009).

In this study, we show that the formation of different metasomatic rocks is associated with fractionation of certain trace-element ratios that otherwise would behave similarly during mantle melting processes. The N-MORB-normalized trace-element ratios of the metasomatic rocks are plotted in Figure 16a. We note that some ratios in the precursor rocks differ from N-MORB, likely reflecting the protolith (pre-subduction) compositions. Moreover, the metasomatic rocks are elevated in Cs/Rb, Cs/Yb, U/Nb, Th/Nb, Sr/Y, La/Sm, and Lu/Hf relative to the precursor. The opposite trend is observed in Hf/Nd, Pb/Ce, Zr/Sm, Sm/Nd, Sr/Nd, and Rb/Sr, where the metasomatic rocks record lower values compared to the precursor. Lastly, the ratios U/Th, Zr/Hf, Dy/Yb, Nb/Ta, Ba/Rb, and U/Pb of the metasomatic rocks are similar to both the precursor and to N-MORB. The Ba/Th ratio is similarly low in metasomatic and precursor rocks, relative to N-MORB. These imply that diffusive metasomatism can induce bulk-rock trace-element fractionations that are typically attributed to both melting and dehydration processes in subduction zones.

One notable observation is the lower Zr/Sm, Hf/Nd, and Th/Nb ratios in chlorite-amphibole schists (Zone II) and chlorite schists (Zone III) relative to the Zones IV and V metagabbro. This marked decrease in these ratios involves the localized mobilization of commonly assumed “fluid-immobile” elements Zr, Hf, and Nb into the adjacent zones (Brenan et al., 1994; Kessel et al., 2005; Stalder et al., 1998). This localized mobilization is due to the destabilization of rutile (hosting Nb) and zircon (hosting Zr and Hf) in these metasomatic rocks. The destabilization of zircon is consistent with previous observation in the Franciscan Complex (USA) where zircon was inferred to be less stable in ultramafic compositions (King et al., 2003). The destabilization of rutile is supported by our thermodynamic models that predict rutile

stability over a wide range of  $P$ - $T$  conditions for bulk compositions similar to an oceanic oxide gabbro. We emphasize that the breakdown of these phases, notably rutile and zircon, in these metasomatic rocks resulted from the changes in bulk compositions and not from changes in pressure and temperature conditions. These fractionations are further enhanced by the diffusion and redistribution of REE from Zones II and III into Zone IV.

Another important observation is the lower Pb/Ce and Sr/Nd ratios in metasomatic rocks, particularly in chlorite-rich schists (Zone III) (Figure 16a). The depletions in Pb and Sr in chlorite schists are likely due to the crystal-chemical control of chlorite, lacking crystallographic sites for  $\text{Ca}^{2+}$ , which is typically substituted for by  $\text{Sr}^{2+}$  and  $\text{Pb}^{2+}$  (Spandler et al., 2014). Whereas Sr and Pb from Zones II and III may have back-diffused into Zone IV, this process did not significantly fractionate the bulk-rock Sr/Nd and Pb/Ce ratios of Zone IV relative to the most distal metagabbro. Thus, the formation of chlorite schists in between serpentinites and crustal rocks may preferentially liberate certain trace elements, such as Sr and Pb. As noted earlier, the co-diffusion of Ca, LREE, Sr and Pb led to the formation of Ca-rich minerals (e.g., epidote) nearby that then became important hosts for these trace elements and prevented their further mobilization. The fractionations in parent-daughter elements Rb/Sr, Sm/Nd and Lu/Hf are important as their Sr, Nd, and Hf isotope compositions will change over time due to radiogenic ingrowth. These isotopically distinct reservoirs can reside in the mantle and may even be sampled and recorded in the erupted mantle-derived magmas. Accordingly, the decrease in Sm/Nd and Rb/Sr ratios, and the increase in Lu/Hf ratio in metasomatic rocks relative to their precursor may lead to their time-integrated evolution to less radiogenic Nd and Sr isotopes, and more radiogenic Hf isotope compositions in the mantle.

In contrast, the lack of substantial modal, chemical, and Sr isotope changes in serpentinite domains suggest a pinned geochemical boundary condition in which the fluids buffered by serpentinite represent a large reservoir that is minimally affected by mass transfer from the juxtaposed metagabbro block. This scenario is possible if

there is enough advective flow in the serpentinite matrix to keep fluid compositions relatively constant within the serpentinite domain. Another possibility is if diffusion through the serpentinite occurs relatively fast, which would transport solutes over larger length scales in the serpentinite than the length scales we observed for the metacrystal block (Ague, 2007; Ague & Rye, 1999). The spatially limited enrichment in  $(\text{La}/\text{Sm})_N$  in the most proximal serpentinite argues against fast diffusion rates of solutes through serpentinite for these elements. It is more likely that overall constancy in serpentinite composition in this study reflects a limited interconnected pore fluid in serpentinite that, in turn, limited diffusive transport across large length scales. The lack of significant enrichment in fluid-mobile elements in serpentinite argues against pervasive advective fluid flow within the serpentinite domain.

Physical mixing of different subducted materials and mantle rocks along the slab-mantle interface has been proposed as a key process in the formation of arc magmas (King et al., 2006; Marschall & Schumacher, 2012; Nielsen & Marschall, 2017). Geodynamic models have predicted the transport of intimately mixed materials (i.e., *mélange*) by buoyant diapirs into the mantle wedge, feeding the source of arc magmas (Gerya & Yuen, 2003; Zhu et al., 2009). The metasomatic reaction zone studied here records a decrease in bulk density associated with the transformation of a dry and dense metacrystal rock into a hydrous and less dense metasomatic rock. These results can be used to infer what could happen to subducted crustal rocks along the slab-mantle interface during subduction because the *P-T* conditions recorded by these rocks are relevant to cold and intermediate slab-top geotherms (Syracuse et al., 2010). The decrease in bulk densities during mass transfer would allow for dense subducted rocks to become positively buoyant relative to the overlying peridotite wedge (Figures 16b and 16c). The metasomatic reaction zone studied here records a decrease in bulk density associated with the transformation of a dry and dense metacrystal rock into a hydrous and less dense metasomatic rock, albeit over limited spatial scales. If this process were more extensive, the decrease in bulk densities during mass transfer would allow for dense subducted rocks to become positively buoyant relative to the overlying peridotite wedge (Figures 16b and 16c). For instance, ~50% of a crustal precursor has to be converted into chlorite schists to make the entire block positively buoyant relative to the overlying mantle with a density of 3300 kg/m<sup>3</sup>. Chlorite schist occupies a small volume in the studied transect, similar to other settings where serpentinite and metacrystal rock are juxtaposed (Angiboust et al., 2014; Bebout & Barton, 2002; Breeding et al., 2004; Gyomlai et al., 2021; Miller et al., 2009; Penniston-Dorland et al., 2014; Spandler et al., 2008). This may be due to an arrested reaction, for example, as the reactant fluid was completely consumed, or by cooling during exhumation (Pogge von Strandmann et al., 2015; Starr et al., 2020). The mechanical weakening of the reacted metacrystal rocks could localize both strain and fluid flow, further enhancing metasomatic reactions (Ague, 2007; Angiboust et al., 2011). If Mg-metasomatism of gabbro is more extensive than in the outcrop that we studied, buoyant metasomatic rocks could result in their detachment and rise as *mélange* diapirs from the slab-top to the overlying mantle, effectively delivering the compositional signatures of these rocks to the source of arc magmas (Codillo et al., 2018; Cruz-Uribe et al., 2018; Marschall & Schumacher, 2012). Fluids that are released during the high-temperature breakdown of Mg-chlorite (>800°C) can promote the partial melting of adjacent mafic crustal rocks within the *mélange*. Melting of rising *mélange* diapirs would further enhance the fractionated trace-element characteristics of the resulting partial melts (Cruz-Uribe et al., 2018).

## 5. Conclusions

Within the context of a serpentinite-metagabbro contact from the Voltri Massif (Italy), we evaluated the fluid-mediated mass transfer processes between mafic and ultramafic rocks in subducted oceanic lithosphere. In oceanic settings, diffusional metasomatism is particularly important at mid-ocean ridge settings of slow-spreading oceanic lithosphere where large chemical potential gradients of chemical species exist in juxtaposed mafic and ultramafic rocks resulting in significant mass transfer such as rodingitization, blackwall alteration, and steatitization. Metasomatic processes between mafic and ultramafic rocks can also occur in subduction zones; however, as this study documents, the elevated pressure and temperature conditions in subduction zones can modulate the speciation of fluids and saturation state of key minerals such as chlorite and talc. One of the main metasomatic processes documented in this study was mass transfer of Mg from serpentinite into gabbro that started during prograde metamorphism and likely continued through peak and retrograde conditions. In contrast to oceanic settings, our thermodynamic models predict the predominance of aqueous Mg species in fluids that equilibrate with serpentinite under high-pressure subduction zone conditions. Consistent with the observed Mg-metasomatism,



our reaction-path models predict that fluids in equilibrium with serpentinite at high-pressure conditions are more strongly enriched in dissolved Mg compared to low-pressure conditions. Therefore, Mg-metasomatism of crustal rocks to form chlorite-rich assemblages is favored in subduction zones. In contrast, Si-metasomatism of serpentinites to form talc-rich rocks (steatitization) is commonly found in oceanic settings, but is predicted to be less prevalent in subduction zones. This illustrates a different picture on the nature and styles of boundary metasomatism at high  $P$ - $T$  conditions, such as in subduction zones, as compared to low  $P$ - $T$  oceanic settings.

Metasomatism can lead to destabilization of trace element-rich phases. Collectively, the dissolution of phases such as rutile and zircon during metasomatism in subduction zones can result in trace-element fractionations (e.g., Th/Nb, Zr/Sm, Hf/Nd) that are otherwise attributed to metamorphic dehydration and melting reactions. Because of the widespread occurrence of juxtaposed mafic and ultramafic rocks in subducting slabs, the slab-mantle interface, and the mantle wedge, metasomatism between these rocks may further enhance trace-element fractionation.

### Data Availability Statement

The data and models that support the findings of this study are freely available in the data repository <https://doi.org/10.5281/zenodo.6611548>.

### Acknowledgments

The authors would like to thank Dr. Jim Eckert (Yale) and Dr. Neel Chatterjee (MIT) for EPMA assistance, and Caitlin Brown (BC) for assistance in the Sr isotope measurements. E.A. Codillo would like to thank Dr. James Andrew Leong (LDEO) for discussion on the DEW model. M. Scambelluri acknowledges the Italian Ministry of Research MUR for granting the PRIN project n. 2017ZE49E7. This research was funded by NSF-OISE (Office of International Science & Engineering, Petrology & Geochemistry) PIRE, Award #1545903, and the WHOI Ocean Ventures Fund.

### References

- Abers, G. A., Keken, P. E., van Kneller, E. A., Ferris, A., & Stachnik, J. C. (2006). The thermal structure of subduction zones constrained by seismic imaging: Implications for slab dehydration and wedge flow. *Earth and Planetary Science Letters*, *241*(3–4), 387–397. <https://doi.org/10.1016/j.epsl.2005.11.055>
- Abers, G. A., van Keken, P. E., & Wilson, C. R. (2020). Deep decoupling in subduction zones: Observations and temperature limits. *Geosphere*, *16*(6), 1408–1424. <https://doi.org/10.1130/GES02278.1>
- Ague, J. J. (2007). Models of permeability contrasts in subduction zone mélange: Implications for gradients in fluid fluxes, Syros and Tinos Islands, Greece. *Chemical Geology*, *239*(3–4), 217–227. <https://doi.org/10.1016/j.chemgeo.2006.08.012>
- Ague, J. J. (2017). Element mobility during regional metamorphism in crustal and subduction zone environments with a focus on the rare Earth elements (REE). *American Mineralogist*, *102*(9), 1796–1821. <https://doi.org/10.2138/am-2017-6130>
- Ague, J. J., & Nicolescu, S. (2014). Carbon dioxide released from subduction zones by fluid-mediated reactions. *Nature Geoscience*, *7*(5), 355–360. <https://doi.org/10.1038/ngeo2143>
- Ague, J. J., & Rye, D. M. (1999). Simple models of CO<sub>2</sub> release from metacarbonates with implications for interpretation of directions and magnitudes of fluid flow in the deep crust. *Journal of Petrology*, *40*(9), 1443–1462. <https://doi.org/10.1093/ptro/40.9.1443>
- Angiboust, S., Agard, P., Raimbourg, H., Yamato, P., & Huet, B. (2011). Subduction interface processes recorded by eclogite-facies shear zones (Monviso, W. Alps). *Lithos*, *127*(1–2), 222–238. <https://doi.org/10.1016/j.lithos.2011.09.004>
- Angiboust, S., Agard, P., Yamato, P., & Raimbourg, H. (2012). Eclogite breccias in a subducted ophiolite: A record of intermediate-depth earthquakes? *Geology*, *40*(8), 707–710. <https://doi.org/10.1130/G32925.1>
- Angiboust, S., Pettke, T., Hoog, J. C. M. D., Caron, B., & Oncken, O. (2014). Channelized fluid flow and eclogite-facies metasomatism along the subduction shear zone. *Journal of Petrology*, *55*(5), 883–916. <https://doi.org/10.1093/ptrology/egu010>
- Bach, W., Garrido, C. J., Paulick, H., Harvey, J., & Rosner, M. (2004). Seawater-peridotite interactions: First insights from ODP leg 209, MAR 15°N. *Geochemistry, Geophysics, Geosystems*, *5*(9). <https://doi.org/10.1029/2004GC000744>
- Bach, W., Jöns, N., & Klein, F. (2013). Metasomatism within the ocean crust. In D. E. Harlow & H. Austrheim (Eds.), *Metasomatism and the chemical transformation of rock: The role of fluids in terrestrial and extraterrestrial processes*. Springer Berlin Heidelberg. (pp. 253–288). [https://doi.org/10.1007/978-3-642-28394-9\\_8](https://doi.org/10.1007/978-3-642-28394-9_8)
- Bach, W., & Klein, F. (2009). The petrology of seafloor rodingites: Insights from geochemical reaction path modeling. *Lithos*, *112*(1–2), 103–117. <https://doi.org/10.1016/j.lithos.2008.10.022>
- Bebout, G., & Barton, M. (2002). Tectonic and metasomatic mixing in a high- $T$ , subduction-zone M? Lange—Insights into the geochemical evolution of the slab-mantle interface. *Chemical Geology*, *187*(1–2), 79–106. [https://doi.org/10.1016/S0009-2541\(02\)00019-0](https://doi.org/10.1016/S0009-2541(02)00019-0)
- Bebout, G. E. (2007). Metamorphic chemical geodynamics of subduction zones. *Earth and Planetary Science Letters*, *260*(3–4), 373–393. <https://doi.org/10.1016/j.epsl.2007.05.050>
- Bebout, G. E., & Penniston-Dorland, S. C. (2016). Fluid and mass transfer at subduction interfaces—The field metamorphic record. *Lithos*, *240–243*, 228–258. <https://doi.org/10.1016/j.lithos.2015.10.007>
- Becker, H., Jochum, K. P., & Carlson, R. W. (2000). Trace element fractionation during dehydration of eclogites from high-pressure terranes and the implications for element fluxes in subduction zones. *Chemical Geology*, *163*(1–4), 65–99. [https://doi.org/10.1016/S0009-2541\(99\)00071-6](https://doi.org/10.1016/S0009-2541(99)00071-6)
- Bickle, M. J., & McKenzie, D. (1987). The transport of heat and matter by fluids during metamorphism. *Contributions to Mineralogy and Petrology*, *95*(3), 384–392. <https://doi.org/10.1007/BF00371852>
- Bloch, S., & Hofmann, A. W. (1978). Magnesium metasomatism during hydrothermal alteration of new oceanic crust. *Geology*, *6*(5), 275–277. [https://doi.org/10.1130/0091-7613\(1978\)6<275:mmdhao>2.0.co;2](https://doi.org/10.1130/0091-7613(1978)6<275:mmdhao>2.0.co;2)
- Boschi, C., Früh-Green, G. L., Delacour, A., Karson, J. A., & Kelley, D. S. (2006). Mass transfer and fluid flow during detachment faulting and development of an oceanic core complex, Atlantis Massif (MAR 30°N). *Geochemistry, Geophysics, Geosystems*, *7*(1). <https://doi.org/10.1029/2005GC001074>
- Breeding, C. M., Ague, J. J., & Bröcker, M. (2004). Fluid–metasedimentary rock interactions in subduction-zone mélange: Implications for the chemical composition of arc magmas. *Geology*, *32*(12), 1041–1044. <https://doi.org/10.1130/G20877.1>
- Brenan, J. M., Shaw, H. F., Phinney, D. L., & Ryerson, F. J. (1994). Rutile-aqueous fluid partitioning of Nb, Ta, Hf, Zr, U and Th: Implications for high field strength element depletions in island-arc basalts. *Earth and Planetary Science Letters*, *128*(3–4), 327–339. [https://doi.org/10.1016/0012-821X\(94\)90154-6](https://doi.org/10.1016/0012-821X(94)90154-6)

- Cannaò, E., Scambelluri, M., Agostini, S., Tonarini, S., & Godard, M. (2016). Linking serpentinite geochemistry with tectonic evolution at the subduction plate-interface: The Voltri Massif case study (Ligurian Western Alps, Italy). *Geochimica et Cosmochimica Acta*, *190*, 115–133. <https://doi.org/10.1016/j.gca.2016.06.034>
- Carlson, W. D., Pattison, D. R. M., & Caddick, M. J. (2015). Beyond the equilibrium paradigm: How consideration of kinetics enhances metamorphic interpretation. *American Mineralogist*, *100*(8–9), 1659–1667. <https://doi.org/10.2138/am-2015-5097>
- Carter, L. B., Skora, S., Blundy, J. D., De Hoog, J. C. M., & Elliott, T. (2015). An experimental study of trace element fluxes from subducted oceanic crust. *Journal of Petrology*, *56*(8), 1585–1606. <https://doi.org/10.1093/ptrology/egv046>
- Codillo, E. (2022). Fluid-mediated interactions between serpentinite and gabbro: Fluid speciation and reaction-path models. <https://doi.org/10.5281/zenodo.6611549>
- Codillo, E. A., Le Roux, V., & Marschall, H. R. (2018). Arc-like magmas generated by mélange-peridotite interaction in the mantle wedge. *Nature Communications*, *9*(1), 2864. <https://doi.org/10.1038/s41467-018-05313-2>
- Connolly, J. A. D. (2009). The geodynamic equation of state: What and how. *Geochemistry, Geophysics, Geosystems*, *10*. <https://doi.org/10.1029/2009GC002540>
- Cooperdock, E. H. G., Raia, N. H., Barnes, J. D., Stockli, D. F., & Schwarzenbach, E. M. (2018). Tectonic origin of serpentinites on Syros, Greece: Geochemical signatures of abyssal origin preserved in a HP/LT subduction complex. *Lithos*, *296–299*, 352–364. <https://doi.org/10.1016/j.lithos.2017.10.020>
- Cruz-Urbe, A. M., Marschall, H. R., Gaetani, G. A., & Le Roux, V. (2018). Generation of alkaline magmas in subduction zones by partial melting of mélange diapirs—An experimental study. *Geology*, *46*(4), 343–346. <https://doi.org/10.1130/G39956.1>
- Debret, B., Andreani, M., Muñoz, M., Bolfan-Casanova, N., Carlut, J., Nicollet, C., et al. (2014). Evolution of Fe redox state in serpentine during subduction. *Earth and Planetary Science Letters*, *400*, 206–218. <https://doi.org/10.1016/j.epsl.2014.05.038>
- Debret, B., Millet, M.-A., Pons, M.-L., Bouilhol, P., Inglis, E., & Williams, H. (2016). Isotopic evidence for iron mobility during subduction. *Geology*, *44*(3), 215–218. <https://doi.org/10.1130/G37565.1>
- Deschamps, F., Godard, M., Guillot, S., & Hattori, K. (2013). Geochemistry of subduction zone serpentinites: A review. *Lithos*, *178*, 96–127. <https://doi.org/10.1016/j.lithos.2013.05.019>
- Diener, J. F. A., & Powell, R. (2010). Influence of ferric iron on the stability of mineral assemblages. *Journal of Metamorphic Geology*, *28*(6), 599–613. <https://doi.org/10.1111/j.1525-1314.2010.00880.x>
- Douville, E., Charlou, J. L., Oelkers, E. H., Bienvenu, P., Colon, C. F. J., Donval, J. P., et al. (2002). The rainbow vent fluids (36°14'N, MAR): The influence of ultramafic rocks and phase separation on trace metal content in Mid-Atlantic Ridge hydrothermal fluids. *Chemical Geology*, *184*(1–2), 37–48. [https://doi.org/10.1016/S0009-2541\(01\)00351-5](https://doi.org/10.1016/S0009-2541(01)00351-5)
- Dragovic, B., Samanta, L. M., Baxter, E. F., & Selverstone, J. (2012). Using garnet to constrain the duration and rate of water-releasing metamorphic reactions during subduction: An example from Sifnos, Greece. *Chemical Geology*, *314–317*, 9–22. <https://doi.org/10.1016/j.chemgeo.2012.04.016>
- Elderfield, H., & Greaves, M. J. (1982). The rare Earth elements in seawater. *Nature*, *296*(5854), 214–219. <https://doi.org/10.1038/296214a0>
- Evans, K. A., & Frost, B. R. (2021). Deserpentinization in subduction zones as a source of oxidation in arcs: A reality check. *Journal of Petrology*, *62*(3). <https://doi.org/10.1093/ptrology/egab016>
- Federico, L., Capponi, G., Crispini, L., Scambelluri, M., & Villa, I. (2005). <sup>39</sup>Ar/<sup>40</sup>Ar dating of high-pressure rocks from the Ligurian Alps: Evidence for a continuous subduction? Exhumation cycle. *Earth and Planetary Science Letters*, *240*(3–4), 668–680. <https://doi.org/10.1016/j.epsl.2005.09.062>
- Federico, L., Crispini, L., Malatesta, C., Torchio, S., & Capponi, G. (2015). Geology of the Pontinvrea area (Ligurian Alps, Italy): Structural setting of the contact between Montenotte and Voltri units. *Journal of Maps*, *11*(1), 101–113. <https://doi.org/10.1080/17445647.2014.945749>
- Federico, L., Crispini, L., Scambelluri, M., & Capponi, G. (2007). Ophiolite mélange zone records exhumation in a fossil subduction channel. *Geology*, *35*(6), 499–502. <https://doi.org/10.1130/G23190A.1>
- Ferry, J. M., & Dipple, G. M. (1991). Fluid flow, mineral reactions, and metasomatism. *Geology*, *19*(3), 211–214. [https://doi.org/10.1130/0091-7613\(1991\)019<0211:ffmram>2.3.co;2](https://doi.org/10.1130/0091-7613(1991)019<0211:ffmram>2.3.co;2)
- Fryer, P. (2012). Serpentinite mud volcanism: Observations, processes, and implications. *Annual Review of Marine Science*, *4*(1), 345–373. <https://doi.org/10.1146/annurev-marine-120710-100922>
- Gale, A., Dalton, C. A., Langmuir, C. H., Su, Y., & Schilling, J.-G. (2013). The mean composition of ocean ridge basalts. *Geochemistry, Geophysics, Geosystems*, *14*(3), 489–518. <https://doi.org/10.1029/2012GC004334>
- German, C. R., & Elderfield, H. (1990). Application of the Ce anomaly as a paleoredox indicator: The ground rules. *Paleoceanography*, *5*, 823–833. <https://doi.org/10.1029/PA005i005p00823>
- Gerya, T., & Stöckhert, B. (2006). Two-dimensional numerical modeling of tectonic and metamorphic histories at active continental margins. *International Journal of Earth Sciences*, *95*(2), 250–274. <https://doi.org/10.1007/s00531-005-0035-9>
- Gerya, T. V., & Yuen, D. A. (2003). Rayleigh–Taylor instabilities from hydration and melting propel “cold plumes” at subduction zones. *Earth and Planetary Science Letters*, *212*(1–2), 47–62. [https://doi.org/10.1016/S0012-821X\(03\)00265-6](https://doi.org/10.1016/S0012-821X(03)00265-6)
- Godard, M., Awaji, S., Hansen, H., Hellebrand, E., Brunelli, D., Johnson, K., et al. (2009). Geochemistry of a long in-situ section of intrusive slow-spread oceanic lithosphere: Results from IODP Site U1309 (Atlantis Massif, 30°N Mid-Atlantic-Ridge). *Earth and Planetary Science Letters*, *279*(1–2), 110–122. <https://doi.org/10.1016/j.epsl.2008.12.034>
- Gorman, J. K., Penniston-Dorland, S. C., Marschall, H. R., & Walker, R. J. (2019). The roles of mechanical mixing and fluid transport in the formation of reaction zones in subduction-related mélange: Evidence from highly siderophile elements. *Chemical Geology*, *525*, 96–111. <https://doi.org/10.1016/j.chemgeo.2019.07.004>
- Groppo, C., Beltrando, M., & Compagnoni, R. (2009). The P–T path of the ultra-high pressure Lago di Cignana and adjoining high-pressure meta-ophiolitic units: Insights into the evolution of the subducting Tethyan slab. *Journal of Metamorphic Geology*, *27*(3), 207–231. <https://doi.org/10.1111/j.1525-1314.2009.00814.x>
- Groppo, C., Rinaudo, C., Cairo, S., Gastaldi, D., & Compagnoni, R. (2006). Micro-Raman spectroscopy for a quick and reliable identification of serpentine minerals from ultramafics. *European Journal of Mineralogy*, *18*(3), 319–329. <https://doi.org/10.1127/0935-1221/2006/0018-0319>
- Guillot, S., Hattori, K., Agard, P., Schwartz, S., & Vidal, O. (2009). Exhumation processes in oceanic and continental subduction contexts: A review, in: In S. Lallemand & F. Funiciello (Eds.), *Subduction zone Geodynamics*. Springer Berlin Heidelberg. (pp. 175–205). [https://doi.org/10.1007/978-3-540-87974-9\\_10](https://doi.org/10.1007/978-3-540-87974-9_10)
- Gyomlai, T., Agard, P., Marschall, H. R., Jolivet, L., & Gerdes, A. (2021). Metasomatism and deformation of block-in-matrix structures in Syros: The role of inheritance and fluid-rock interactions along the subduction interface. *Lithos*, *386–387*, 105996. <https://doi.org/10.1016/j.lithos.2021.105996>
- Hacker, B. R. (2008). H<sub>2</sub>O subduction beyond arcs. *Geochemistry, Geophysics, Geosystems*, *9*(3). <https://doi.org/10.1029/2007GC001707>

- Harlow, G. E., Flores, K. E., & Marschall, H. R. (2016). Fluid-mediated mass transfer from a paleosubduction channel to its mantle wedge: Evidence from Jadeite and related rocks from the Guatemala Suture Zone. *Lithos*, 258, 15–36. <https://doi.org/10.1016/j.lithos.2016.04.010>
- Haws, A. A., Starr, P. G., Dragovic, B., Scambelluri, M., Belmonte, D., Caddick, M. J., et al. (2021). Meta-rodingite dikes as recorders of subduction zone metamorphism and serpentinite dehydration: Voltri Ophiolite, Italy. *Chemical Geology*, 565, 120077. <https://doi.org/10.1016/j.chemgeo.2021.120077>
- Hawthorne, F. C., Oberti, R., Harlow, G. E., Maresch, W. V., Martin, R. F., Schumacher, J. C., & Welch, M. D. (2012). Nomenclature of the amphibole supergroup. *American Mineralogist*, 97(11–12), 2031–2048. <https://doi.org/10.2138/am.2012.4276>
- Holland, T. J. B., & Powell, R. (1998). An internally consistent thermodynamic data set for phases of petrological interest. *Journal of Metamorphic Geology*, 16(3), 309–343. <https://doi.org/10.1111/j.1525-1314.1998.00140.x>
- Honnorez, J., & Kirst, P. (1975). Petrology of rodingites from the equatorial Mid-Atlantic fracture zones and their geotectonic significance. *Contributions to Mineralogy and Petrology*, 49(3), 233–257. <https://doi.org/10.1007/bf00376590>
- Huang, F., & Sverjensky, D. A. (2019). Extended deep earth water model for predicting major element mantle metasomatism. *Geochimica et Cosmochimica Acta*, 254, 192–230. <https://doi.org/10.1016/j.gca.2019.03.027>
- Humphris, S. E., & Thompson, G. (1978). Hydrothermal alteration of oceanic basalts by seawater. *Geochimica et Cosmochimica Acta*, 42(1), 107–125. [https://doi.org/10.1016/0016-7037\(78\)90221-1](https://doi.org/10.1016/0016-7037(78)90221-1)
- Hunziker, J. C. (1974). Rb–Sr and K–Ar age determination and the Alpine tectonic history of the Western Alps.
- Iacovino, K., Guild, M. R., & Till, C. B. (2020). Aqueous fluids are effective oxidizing agents of the mantle in subduction zones. *Contributions to Mineralogy and Petrology*, 175(4), 36. <https://doi.org/10.1007/s00410-020-1673-4>
- John, T., Scherer, E. E., Haase, K., & Schenk, V. (2004). Trace element fractionation during fluid-induced eclogitization in a subducting slab: Trace element and Lu–Hf–Sm–Nd isotope systematics. *Earth and Planetary Science Letters*, 227(3–4), 441–456. <https://doi.org/10.1016/j.epsl.2004.09.009>
- Jones, C. E., Jenkyns, H. C., Coe, A. L., & Stephen, H. P. (1994). Strontium isotopic variations in Jurassic and Cretaceous seawater. *Geochimica et Cosmochimica Acta*, 58(14), 3061–3074. [https://doi.org/10.1016/0016-7037\(94\)90179-1](https://doi.org/10.1016/0016-7037(94)90179-1)
- Kessel, R., Schmidt, M. W., Ulmer, P., & Pettko, T. (2005). Trace element signature of subduction-zone fluids, melts and supercritical liquids at 120–180 km depth. *Nature*, 437(7059), 724–727. <https://doi.org/10.1038/nature03971>
- King, R. L., Bebout, G. E., Moriguti, T., & Nakamura, E. (2006). Elemental mixing systematics and Sr–Nd isotope geochemistry of mélange formation: Obstacles to identification of fluid sources to arc volcanics. *Earth and Planetary Science Letters*, 246(3–4), 288–304. <https://doi.org/10.1016/j.epsl.2006.03.053>
- King, R. L., Kohn, M. J., & Eiler, J. M. (2003). Constraints on the petrologic structure of the subduction zone slab–mantle interface from Franciscan Complex exotic ultramafic blocks. *GSA Bulletin*, 115(9), 1097–1109. <https://doi.org/10.1130/B25255.1>
- Kirby, S., Engdahl, R. E., & Denlinger, R. (2013). Intermediate-depth intraslab earthquakes and arc volcanism as physical expressions of crustal and uppermost mantle metamorphism in subducting slabs. In *Subduction*. American Geophysical Union (AGU). (pp. 195–214). <https://doi.org/10.1029/GM096p0195>
- Klein, F., Bach, W., Humphris, S. E., Kahl, W.-A., Jöns, N., Moskowicz, B., & Berquó, T. S. (2014). Magnetite in seafloor serpentinite—Some like it hot. *Geology*, 42(2), 135–138. <https://doi.org/10.1130/G35068.1>
- Klein, F., Bach, W., Jöns, N., McCollom, T., Moskowicz, B., & Berquó, T. (2009). Iron partitioning and hydrogen generation during serpentinization of abyssal peridotites from 15°N on the Mid-Atlantic Ridge. *Geochimica et Cosmochimica Acta*, 73(22), 6868–6893. <https://doi.org/10.1016/j.gca.2009.08.021>
- Klein, F., Humphris, S., & Bach, W. (2020). Brucite formation and dissolution in oceanic serpentinite. *Geochemical Perspectives Letters*, 16, 1–5. <https://doi.org/10.7185/geochemlet.2035>
- Klein, F., Marschall, H. R., Bowring, S. A., Humphris, S. E., & Horning, G. (2017). Mid-Ocean Ridge serpentinite in the Puerto Rico trench: From seafloor spreading to subduction. *Journal of Petrology*, 58(9), 1729–1754. <https://doi.org/10.1093/petrology/egx071>
- Kodolányi, J., Pettko, T., Spandler, C., Kamber, B. S., & Gmélíng, K. (2012). Geochemistry of ocean floor and fore-arc serpentinites: Constraints on the ultramafic Input to subduction zones. *Journal of Petrology*, 53(2), 235–270. <https://doi.org/10.1093/petrology/egr058>
- Korzhinskii, D. S. (1965). The theory of systems with perfectly mobile components and processes of mineral formation. *American Journal of Science*, 263(3), 193–205. <https://doi.org/10.2475/ajs.263.3.193>
- Korzhinskii, D. S. (1968). The theory of metasomatic zoning. *Mineralium Deposita*, 3, 222–231. <https://doi.org/10.1007/BF00207435>
- Lagabrielle, Y., & Lemoine, M. (1997). Alpine, Corsican and Apennine Ophiolites: The slow-spreading ridge model. *Comptes Rendus de l'Académie des Sciences—Series IIA: Earth and Planetary Science*, 325(12), 909–920. [https://doi.org/10.1016/S1251-8050\(97\)82369-5](https://doi.org/10.1016/S1251-8050(97)82369-5)
- Malatesta, C., Crispini, L., Federico, L., Capponi, G., & Scambelluri, M. (2012a). The exhumation of high pressure ophiolites (Voltri Massif, Western Alps): Insights from structural and petrologic data on metagabbro bodies. *Tectonophysics*, 568–569, 102–123. <https://doi.org/10.1016/j.tecto.2011.08.024>
- Malatesta, C., Crispini, L., Federico, L., Capponi, G., & Scambelluri, M. (2012b). The exhumation of high pressure ophiolites (Voltri Massif, Western Alps): Insights from structural and petrologic data on metagabbro bodies. *Tectonophysics*, 568–569, 102–123. <https://doi.org/10.1016/j.tecto.2011.08.024>
- Manatschal, G., & Müntener, O. (2009). A type sequence across an ancient magma-poor ocean–continent transition: The example of the Western Alpine Tethys ophiolites. *Tectonophysics*, 473(1–2), 4–19. <https://doi.org/10.1016/j.tecto.2008.07.021>
- Manning, C. (2007). Solubility of corundum + kyanite in H<sub>2</sub>O at 700°C and 10 kbar: Evidence for Al<sub>2</sub>Si complexing at high pressure and temperature. *Geofluids*, 7(2), 258–269. <https://doi.org/10.1111/j.1468-8123.2007.00179.x>
- Marschall, H., Altherr, R., Gmélíng, K., & Kasztovszky, Z. (2009). Lithium, boron and chlorine as tracers for metasomatism in high-pressure metamorphic rocks: A case study from Syros (Greece). *Mineralogy and Petrology*, 95(3–4), 291–302. <https://doi.org/10.1007/s00710-008-0032-3>
- Marschall, H. R., & Schumacher, J. C. (2012). Arc magmas sourced from mélange diapirs in subduction zones. *Nature Geoscience*, 5(12), 862–867. <https://doi.org/10.1038/ngeo1634>
- McDonough, W. F., & Sun, S.-s. (1995). The composition of the Earth. *Chemical Geology*, 120(3–4), 223–253. [https://doi.org/10.1016/0009-2541\(94\)00140-4](https://doi.org/10.1016/0009-2541(94)00140-4)
- Messiga, B., Piccardo, G. B., & Ernst, W. G. (1983). High-pressure Eo-Alpine parageneses developed in magnesian metagabbros, Gruppo di Voltri, Western Liguria, Italy. *Contributions to Mineralogy and Petrology*, 83(1–2), 1–15. <https://doi.org/10.1007/BF00373074>
- Messiga, B., & Scambelluri, M. (1991). Retrograde P–T–t path for the Voltri Massif eclogites (Ligurian Alps, Italy): Some tectonic implications. *Journal of Metamorphic Geology*, 9(1), 93–109. <https://doi.org/10.1111/j.1525-1314.1991.tb00506.x>
- Miller, D. P., Marschall, H. R., & Schumacher, J. C. (2009). Metasomatic formation and petrology of blueschist-facies hybrid rocks from Syros (Greece): Implications for reactions at the slab–mantle interface. *Lithos*, 107(1–2), 53–67. <https://doi.org/10.1016/j.lithos.2008.07.015>



- Mori, Y., Shigeno, M., & Nishiyama, T. (2014). Fluid-metapelite interaction in an ultramafic mélange: Implications for mass transfer along the slab-mantle interface in subduction zones. *Earth Planets and Space*, 66(1), 47. <https://doi.org/10.1186/1880-5981-66-47>
- Mottl, M. J., Wheat, C. G., Fryer, P., Gharib, J., & Martin, J. B. (2004). Chemistry of springs across the Mariana forearc shows progressive devolatilization of the subducting plate. *Geochimica et Cosmochimica Acta*, 68(23), 4915–4933. <https://doi.org/10.1016/j.gca.2004.05.037>
- Nielsen, S. G., & Marschall, H. R. (2017). Geochemical evidence for mélange melting in global arcs. *Science Advances*, 3(4). <https://doi.org/10.1126/sciadv.1602402>
- Okamoto, A. S., Verberne, B. A., Niemeijer, A. R., Takahashi, M., Shimizu, I., Ueda, T., & Spiers, C. J. (2019). Frictional properties of simulated chlorite gouge at hydrothermal conditions: Implications for subduction megathrusts. *Journal of Geophysical Research: Solid Earth*, 124(5), 4545–4565. <https://doi.org/10.1029/2018JB017205>
- Palin, R. M., Weller, O. M., Waters, D. J., & Dyck, B. (2016). Quantifying geological uncertainty in metamorphic phase equilibria modeling: a Monte Carlo assessment and implications for tectonic interpretations. *Geoscience Frontiers*, 7(4), 591–607. <https://doi.org/10.1016/j.gsf.2015.08.005>
- Paulick, H., Bach, W., Godard, M., De Hoog, J. C. M., Suhr, G., & Harvey, J. (2006). Geochemistry of abyssal peridotites (Mid-Atlantic Ridge, 15°20'N, ODP Leg 209): Implications for fluid/rock interaction in slow spreading environments. *Chemical Geology*, 234(3–4), 179–210. <https://doi.org/10.1016/j.chemgeo.2006.04.011>
- Pawley, A. (2003). Chlorite stability in mantle peridotite: The reaction clinocllore+enstatite=forsterite+pyrope+H<sub>2</sub>O. *Contributions to Mineralogy and Petrology*, 144(4), 449–456. <https://doi.org/10.1007/s00410-002-0409-y>
- Peacock, S. M., & Wang, K. (2021). On the stability of talc in subduction zones: A possible control on the maximum depth of decoupling between the subducting plate and mantle wedge. *Geophysical Research Letters*, 48(17), e2021GL094889. <https://doi.org/10.1029/2021GL094889>
- Penniston-Dorland, S. C., Gorman, J. K., Bebout, G. E., Piccoli, P. M., & Walker, R. J. (2014). Reaction rind formation in the Catalina Schist: Deciphering a history of mechanical mixing and metasomatic alteration. *Chemical Geology*, 384, 47–61. <https://doi.org/10.1016/j.chemgeo.2014.06.024>
- Peters, D., Bretscher, A., John, T., Scambelluri, M., & Pettko, T. (2017a). Fluid-mobile elements in serpentinites: Constraints on serpentinisation environments and element cycling in subduction zones. *Chemical Geology*, 466, 654–666. <https://doi.org/10.1016/j.chemgeo.2017.07.017>
- Peters, D., Bretscher, A., John, T., Scambelluri, M., & Pettko, T. (2017b). Fluid-mobile elements in serpentinites: Constraints on serpentinisation environments and element cycling in subduction zones. *Chemical Geology*, 466, 654–666. <https://doi.org/10.1016/j.chemgeo.2017.07.017>
- Peters, D., Pettko, T., John, T., & Scambelluri, M. (2020). The role of brucite in water and element cycling during serpentinite subduction—Insights from Erro Tobbio (Liguria, Italy). *Lithos*, 360–361, 105431. <https://doi.org/10.1016/j.lithos.2020.105431>
- Petriglieri, J. R., Salvioli-Mariani, E., Mantovani, L., Tribaudino, M., Lottici, P. P., Laporte-Magoni, C., & Bersani, D. (2015). Micro-Raman mapping of the polymorphs of serpentine. *Journal of Raman Spectroscopy*, 46(10), 953–958. <https://doi.org/10.1002/jrs.4695>
- Piccardo, G. B. (2013). Subduction of a fossil slow-ultraslow spreading ocean: A petrology-constrained geodynamic model based on the Voltri Massif, Ligurian Alps, Northwest Italy. *International Geology Review*, 55(7), 787–803. <https://doi.org/10.1080/00206814.2012.746806>
- Pogge von Strandmann, P. A. E., Dohmen, R., Marschall, H. R., Schumacher, J. C., & Elliott, T. (2015). Extreme magnesium isotope fractionation at outcrop scale records the mechanism and rate at which reaction fronts advance. *Journal of Petrology*, 56(1), 33–58. <https://doi.org/10.1093/ptrology/legu070>
- Rampone, E., & Hofmann, A. (2012). A global overview of isotopic heterogeneities in the oceanic mantle. *Lithos*, 148, 247–261. <https://doi.org/10.1016/j.lithos.2012.06.018>
- Sanford, R. F. (1982). Growth of ultramafic reaction zones in greenschist to amphibolite facies metamorphism. *American Journal of Science*, 282(5), 543–616. <https://doi.org/10.2475/ajs.282.5.543>
- Scambelluri, M., Cannaò, E., & Gilio, M. (2019). The water and fluid-mobile element cycles during serpentinite subduction. A review. *European Journal of Mineralogy*, 31(3), 405–428. <https://doi.org/10.1127/ejm/2019/0031-2842>
- Scambelluri, M., Müntener, O., Hermann, J., Piccardo, G. B., & Trommsdorff, V. (1995a). Subduction of water into the mantle: History of an Alpine peridotite. *Geology*, 23(5), 459–462. [https://doi.org/10.1130/0091-7613\(1995\)023<0459:sowitm>2.3.co;2](https://doi.org/10.1130/0091-7613(1995)023<0459:sowitm>2.3.co;2)
- Scambelluri, M., Müntener, O., Hermann, J., Piccardo, G. B., & Trommsdorff, V. (1995b). Subduction of water into the mantle: History of an Alpine peridotite. *Geology*, 23(5), 459–462. [https://doi.org/10.1130/0091-7613\(1995\)023<0459:sowitm>2.3.co;2](https://doi.org/10.1130/0091-7613(1995)023<0459:sowitm>2.3.co;2)
- Scambelluri, M., Piccardo, G. B., Philippot, P., Robbiano, A., & Negretti, L. (1997). High salinity fluid inclusions formed from recycled seawater in deeply subducted Alpine serpentinite. *Earth and Planetary Science Letters*, 148(3–4), 485–499. [https://doi.org/10.1016/S0012-821X\(97\)00043-5](https://doi.org/10.1016/S0012-821X(97)00043-5)
- Scambelluri, M., & Rampone, E. (1999). Mg-metasomatism of oceanic gabbros and its control on Ti-clinohumite formation during eclogitization. *Contributions to Mineralogy and Petrology*, 135, 1–17. <https://doi.org/10.1007/s004100050494>
- Scambelluri, M., Strating, E. H. H., Piccardo, G. B., Vissers, R. L. M., & Rampone, E. (1991). Alpine olivine- and titanite-bearing assemblages in the Erro-Tobbio peridotite (Voltri Massif, NW Italy). *Journal of Metamorphic Geology*, 9(1), 79–91. <https://doi.org/10.1111/j.1525-1314.1991.tb00505.x>
- Schmidt, M. W., & Poli, S. (1998). Experimentally based water budgets for dehydrating slabs and consequences for arc magma generation. *Earth and Planetary Science Letters*, 163(1–4), 361–379. [https://doi.org/10.1016/S0012-821X\(98\)00142-3](https://doi.org/10.1016/S0012-821X(98)00142-3)
- Schmidt, M. W., & Poli, S. (2014). 4.19—Devolatilization during subduction, In *Treatise on geochemistry* (2nd edn). (pp. 669–701). <https://doi.org/10.1016/B978-0-08-095975-7.00321-1>
- Schwarzenbach, E. M., Vogel, M., Früh-Green, G. L., & Boschi, C. (2021). Serpentinization, carbonation, and metasomatism of ultramafic sequences in the Northern Apennine Ophiolite (NW Italy). *Journal of Geophysical Research: Solid Earth*, 126(5), e2020JB020619. <https://doi.org/10.1029/2020JB020619>
- Smye, A. J., Seman, S. M., Scambelluri, M., Starr, P. G., & Federico, L. (2021). Exhumation dynamics of high-pressure metamorphic rocks from the Voltri Unit, Western Alps: Constraints from phengite Rb–Sr geochronology. *Contributions to Mineralogy and Petrology*, 176(2), 14. <https://doi.org/10.1007/s00410-020-01767-0>
- Sorensen, S. S., & Grossman, J. N. (1989). Enrichment of trace elements in garnet amphibolites from a paleo-subduction zone: Catalina Schist, southern California. *Geochimica et Cosmochimica Acta*, 53(12), 3155–3177. [https://doi.org/10.1016/0016-7037\(89\)90096-3](https://doi.org/10.1016/0016-7037(89)90096-3)
- Spandler, C., Hermann, J., Faure, K., Mavrogenes, J. A., & Arculus, R. J. (2008). The importance of talc and chlorite “hybrid” rocks for volatile recycling through subduction zones; evidence from the high-pressure subduction mélange of New Caledonia. *Contributions to Mineralogy and Petrology*, 155(2), 181–198. <https://doi.org/10.1007/s00410-007-0236-2>
- Spandler, C., Pettko, T., & Hermann, J. (2014). Experimental study of trace element release during ultrahigh-pressure serpentinite dehydration. *Earth and Planetary Science Letters*, 391, 296–306. <https://doi.org/10.1016/j.epsl.2014.02.010>

- Stalder, R., Foley, S. F., Brey, G. P., & Horn, I. (1998). Mineral-aqueous fluid partitioning of trace elements at 900–1200°C and 3.0–5.7 GPa: New experimental data for garnet, clinopyroxene, and rutile, and implications for mantle metasomatism. *Geochimica et Cosmochimica Acta*, 62(10), 1781–1801. [https://doi.org/10.1016/S0016-7037\(98\)00101-X](https://doi.org/10.1016/S0016-7037(98)00101-X)
- Starr, P. G., Broadwell, K. S., Dragovic, B., Scambelluri, M., Haws, A. A., Caddick, M. J., et al. (2020). The subduction and exhumation history of the Voltri Ophiolite, Italy: Evaluating exhumation mechanisms for high-pressure metamorphic massifs. *Lithos*, 376–377, 105767. <https://doi.org/10.1016/j.lithos.2020.105767>
- Sverjensky, D. A. (2019). Thermodynamic modelling of fluids from surficial to mantle conditions. *Journal of the Geological Society*, 176(2), 348–374. <https://doi.org/10.1144/jgs2018-105>
- Sverjensky, D. A., Harrison, B., & Azzolini, D. (2014). Water in the deep Earth: The dielectric constant and the solubilities of quartz and corundum to 60kb and 1200°C. *Geochimica et Cosmochimica Acta*, 129, 125–145. <https://doi.org/10.1016/j.gca.2013.12.019>
- Syracuse, E. M., Keken, P. E., & van Abers, G. A. (2010). The global range of subduction zone thermal models. *Physics of the Earth and Planetary Interiors*, 183(1–2), 73–90. <https://doi.org/10.1016/j.pepi.2010.02.004>
- Thompson, A. B. (1975). Calc-silicate diffusion zones between Marble and Pelitic schist. *Journal of Petrology*, 16(1), 314–346. <https://doi.org/10.1093/petrology/16.1.314>
- Thompson, J. B. (1970). Geochemical reaction and open systems. *Geochimica et Cosmochimica Acta*, 34(5), 529–551. [https://doi.org/10.1016/0016-7037\(70\)90015-3](https://doi.org/10.1016/0016-7037(70)90015-3)
- Tostevin, R., Shields, G. A., Tarbuck, G. M., He, T., Clarkson, M. O., & Wood, R. A. (2016). Effective use of cerium anomalies as a redox proxy in carbonate-dominated marine settings. *Chemical Geology*, 438, 146–162. <https://doi.org/10.1016/j.chemgeo.2016.06.027>
- Tribuzio, R., Messiga, B., Vannucci, R., & Bottazzi, P. (1996). Rare Earth element redistribution during high-pressure–low-temperature metamorphism in ophiolitic Fe-gabbros (Liguria, northwestern Italy): Implications for light REE mobility in subduction zones. *Geology*, 24(8), 711–714. [https://doi.org/10.1130/0091-7613\(1996\)024<0711:reerhd>2.3.co;2](https://doi.org/10.1130/0091-7613(1996)024<0711:reerhd>2.3.co;2)
- Tutolo, B. M., Mildner, D. F. R., Gagnon, C. V. L., Saar, M. O., & Seyfried, W. E., Jr. (2016). Nanoscale constraints on porosity generation and fluid flow during serpentinization. *Geology*, 44(2), 103–106. <https://doi.org/10.1130/G37349.1>
- van Keken, P. E., Hacker, B. R., Syracuse, E. M., & Abers, G. A. (2011). Subduction factory: 4. Depth-Dependent flux of H<sub>2</sub>O from subducting slabs worldwide. *Journal of Geophysical Research*, 116(B1), B01401. <https://doi.org/10.1029/2010JB007922>
- Vignaroli, G., Rossetti, F., Bouybaouene, M., Massonne, H.-J., Theye, T., Faccenna, C., & Funicello, R. (2005). A counter-clockwise P–T path for the Voltri massif eclogites (Ligurian Alps, Italy). *Journal of Metamorphic Geology*, 23(7), 533–555. <https://doi.org/10.1111/j.1525-1314.2005.00592.x>
- Vitale Brovarone, A., Sverjensky, D. A., Piccoli, F., Ressico, F., Giovannelli, D., & Daniel, I. (2020). Subduction hides high-pressure sources of energy that may feed the deep subsurface biosphere. *Nature Communications*, 11(1), 3880. <https://doi.org/10.1038/s41467-020-17342-x>
- Wada, I., & Wang, K. (2009). Common depth of slab-mantle decoupling: Reconciling diversity and uniformity of subduction zones. *Geochemistry, Geophysics, Geosystems*, 10. <https://doi.org/10.1029/2009GC002570>
- Watson, E. B., & Baxter, E. F. (2007). Diffusion in solid-Earth systems. *Earth and Planetary Science Letters*, 253(3–4), 307–327. <https://doi.org/10.1016/j.epsl.2006.11.015>
- Whitney, D. L., & Evans, B. W. (2010). Abbreviations for names of rock-forming minerals. *American Mineralogist*, 95(1), 185–187. <https://doi.org/10.2138/am.2010.3371>
- Wolery, T. J. (1992). EQ3/6, a software package for geochemical modeling of aqueous systems: Package overview and installation guide (Version 7.0). <https://doi.org/10.2172/138894>
- Workman, R. K., & Hart, S. R. (2005). Major and trace element composition of the depleted MORB mantle (DMM). *Earth and Planetary Science Letters*, 231(1–2), 53–72. <https://doi.org/10.1016/j.epsl.2004.12.005>
- Zhu, G., Gerya, T. V., Yuen, D. A., Honda, S., Yoshida, T., & Connolly, J. A. D. (2009). Three-dimensional dynamics of hydrous thermal-chemical plumes in oceanic subduction zones. *Geochemistry, Geophysics, Geosystems*, 10(11). <https://doi.org/10.1029/2009GC002625>

## References From the Supporting Information

- Ague, J., & van Haren, J. (1996). Assessing metasomatic mass and volume changes using the bootstrap, with application to deep crustal hydrothermal alteration of marble. *Economic Geology*, 91, 1169–1182. <https://doi.org/10.2113/gsecongeo.91.7.1169>
- Baxter, E. F., & DePaolo, D. J. (2002). Field measurement of high temperature bulk reaction rates II: Interpretation of results from a field site near Simplon Pass, Switzerland. *American Journal of Science*, 302, 465–516. <https://doi.org/10.2475/ajs.302.6.465>
- Coggon, R., & Holland, T. J. B. (2002). Mixing properties of phengitic micas and revised garnet-phengite thermobarometers. *Journal of Metamorphic Geology*, 20, 683–696. <https://doi.org/10.1046/j.1525-1314.2002.00395.x>
- Diener, J. F. A., & Powell, R. (2012). Revised activity–composition models for clinopyroxene and amphibole. *Journal of Metamorphic Geology*, 30, 131–142. <https://doi.org/10.1111/j.1525-1314.2011.00959.x>
- Downs, R. T. (2006). The RRUFF Project: An integrated study of the chemistry, crystallography, Raman and infrared spectroscopy of minerals. *Program and Abstracts of the 19th General Meeting of the International Mineralogical Association in Kobe*.
- Grant, J. A. (1986). The isocon diagram; a simple solution to Gresens' equation for metasomatic alteration. *Economic Geology*, 81, 1976–1982. <https://doi.org/10.2113/gsecongeo.81.8.1976>
- Green, E., Holland, T., & Powell, R. (2007). An order-disorder model for omphacitic pyroxenes in the system jadeite-diopside-hedenbergite-acmite, with applications to eclogitic rocks. *American Mineralogist*, 92, 1181–1189. <https://doi.org/10.2138/am.2007.2401>
- Gresens, R. L. (1967). Composition-volume relationships of metasomatism. *Chemical Geology*, 2, 47–65. [https://doi.org/10.1016/0009-2541\(67\)90004-6](https://doi.org/10.1016/0009-2541(67)90004-6)
- Helgeson, H. C. (1969). Thermodynamics of hydrothermal systems at elevated temperatures and pressures. *American Journal of Science*, 267, 729–804. <https://doi.org/10.2475/ajs.267.7.729>
- Holland, T., & Powell, R. (2003). Activity–composition relations for phases in petrological calculations: An asymmetric multicomponent formulation. *Contributions to Mineralogy and Petrology*, 145, 492–501. <https://doi.org/10.1007/s00410-003-0464-z>
- Lafuente, B., Downs, R. T., Yang, H., & Stone, N. (2015). I. The power of databases: The RRUFF project. *Highlights in Mineralogical Crystallography*, in: In T. Armbruster, & R.M. Danisi (Eds.), De Gruyter (O). (pp. 1–30). <https://doi.org/10.1515/9783110417104-003>
- Lanari, P., & Engi, M. (2017). Local Bulk Composition Effects on Metamorphic Mineral Assemblages. *Reviews in Mineralogy and Geochemistry*, 83, 55–102. <https://doi.org/10.2138/rmg.2017.83.3>
- Penniston-Dorland, S. C., & Ferry, J. M. (2008). Element mobility and scale of mass transport in the formation of quartz veins during regional metamorphism of the Waits River Formation, east-central Vermont. *American Mineralogist*, 93, 7–21. <https://doi.org/10.2138/am.2008.2461>

- White, R. W., Powell, R., & Clarke, G. L. (2002). The interpretation of reaction textures in Fe-rich metapelitic granulites of the Musgrave Block, central Australia: Constraints from mineral equilibria calculations in the system  $K_2O-FeO-MgO-Al_2O_3-SiO_2-H_2O-TiO_2-Fe_2O_3$ . *Journal of Metamorphic Geology*, 20, 41–55. <https://doi.org/10.1046/j.0263-4929.2001.00349.x>
- Zhang, Z., & Duan, Z. (2005). Prediction of the PVT properties of water over wide range of temperatures and pressures from molecular dynamics simulation. *Physics of the Earth and Planetary Interiors*, 149, 335–354. <https://doi.org/10.1016/j.pepi.2004.11.003>